The Katsevich Inversion Formula for Cone-Beam Computed Tomography

Adam J. Wunderlich
Department of Mathematics
Oregon State University

September, 2006

Abstract

This paper examines Katsevich's inversion formula developed in [10, 11, 12] for fully 3-D cone-beam computed tomography (CT) with a helical scanning path. This formula is special because is it both theoretically exact before discretization, and it may be implemented via a filtered-backprojection (FBP) type algorithm. Therefore, it has the potential for both high accuracy and a fast implementation. An introduction to the theory behind the formula, implementation details, and numerical results will be provided.

Acknowledgments

I would like to thank Kyle Champley for many spirited discussions. Also, I would like to thank my advisor, Adel Faridani, for general guidance and for helpful comments regarding this work.

Contents

List of Figures

List of Tables

Chapter 1

Introduction

Computed tomography (CT) is a standard medical imaging technique which first came into clinical use in the 1970's. It uses measured x-ray projections through an object (normally a person or animal) to mathematically reconstruct the x-ray attenuation function of the object. The physical problem may be recast in mathematical terms by saying that we wish to reconstruct an object from its line integrals. This is an example of an "inverse problem" in mathematical jargon.

Classically, CT algorithms reconstruct 2-D slices of an object using either the parallel-beam or fan-beam scanning geometries. Although many types of methods may be used for the reconstruction, the most widely used reconstruction algorithms are part of the filtered back-projection (FBP) family. These algorithms consist of successive 1-D filtering followed by a "back-projection" integral. The FBP algorithms are the most popular because they allow for both fast computation and high accuracy. For more details on classical CT, its variants, and related modalities, the reader is referred to [13] and [14] for a mathematical viewpoint, [9] for an engineering viewpoint, and [16, Ch. 7] for historical references.

With increases in computing power, interest in fully 3-D computed tomography has become a focus. Of course, multiple 2-D reconstructions may be registered to yield a single 3-D volume. However, this technique is undesirable due to the necessarily long acquisition times to obtain many slices. Instead, research efforts have focused on direct 3-D reconstructions. To allow for the rapid acquisition of large amounts of projection data, a three dimensional rectangular cone-shaped x-ray beam together with a 2-D detector array directly opposite the x-ray source has been proposed. CT performed with

such data is termed "cone-beam" computed tomography. Although many types of scanning paths are possible, focus in the clinical setting has been on cone-beam CT using a helical scanning path for the x-ray source. The patient lies on a platform which translates through the rotating source/detector gantry. In this way, the x-ray source traces out a helix around the body of the patient.

In 1984, Feldkamp, Davis, and Kress [7] proposed a filtered back-projection algorithm for cone-beam CT suitable for a circular scanning path. The FDK algorithm may also be easily extended to more general scanning paths, such as a helix, e.g. see Wang et al. [19]. The FDK algorithm is fast and gives reasonable results in some circumstances. However, it is based on an approximate inversion formula (before discretization). Consequently, it is difficult to fully analyze its numerical properties and to predict reconstruction artifacts. Since the FDK algorithm was proposed, a great deal of effort has been invested in looking for faster and more accurate reconstruction methods. Of particular interest are methods based on theoretically exact inversion formulas which are of the FBP type.

Alexander Katsevich made a breakthrough in 2002 with the first of a series of papers [11, 10, 12]. In these papers, he proved a theoretically exact reconstruction formula for helical cone-beam CT which is of the filtered back-projection type.

This paper will introduce Katsevich's result, describe its implementation, and explore its numerical properties. In particular, chapter 2 will explain the Katsevich formula. Next, chapters 3 and 4 will derive numerical implementations of the Katsevich formula for flat and curved detectors, respectively. Chapter 5 will provide numerical results for both the Katsevich and the classical FDK methods, comparing these approaches. Finally, chapter 6 summarizes the conclusions of this paper. MATLAB code for the algorithms is provided in the appendix.

Chapter 2

The Katsevich Inversion Formula

2.1 Some Definitions and Basic Facts

First, we need to set notation and describe some facts necessary to understand Katsevich's result. Bold letters will represent points and vectors in $\mathbb{R}^3$. Also, denote the usual Euclidean inner product by $< \cdot, \cdot >$.

The Fourier transform of a function $f \in L^1(\mathbb{R})$ is defined by

$$\hat{f}(\xi) = \int_{-\infty}^{\infty} f(x) e^{-i2\pi x\xi} dx.$$

Also, the inverse Fourier transform of $\hat{f} \in L^1(\mathbb{R})$ is defined to be

$$f(x) = \int_{-\infty}^{\infty} \hat{f}(\xi) e^{i2\pi x\xi} d\xi.$$

The Fourier transform may be extended to functions in $L^2(\mathbb{R})$ via a limiting process [8, Ch. 13]. The Hilbert transform of a function $f \in L^2(\mathbb{R})$ is defined as

$$\mathcal{H}f(x) = \frac{1}{\pi} PV \int_{-\infty}^{\infty} \frac{f(y)}{x-y} dy,$$

where PV means that the integral should be interpreted as a principal value integral.

We see that the Hilbert transform is a convolution of $f(x)$ with the kernel

$$k_H(t) = \frac{1}{\pi t}.$$

It can be shown that the Fourier Transform of the Hilbert kernel is

$$\hat{k}_H(\xi) = -i \operatorname{sgn}(\xi),$$

e.g. see Natterer [13][p.185-186]. Therefore, the Hilbert transform may be expressed in the Fourier domain via

$$\widehat{\mathcal{H}f}(\xi) = -i \operatorname{sgn}(\xi)\hat{f}(\xi).$$

It is interesting to note that both the Fourier transform and Hilbert transform are isometries on $L^2(\mathbb{R})$.

Let $f(\mathbf{x}) \in C^\infty(\mathbb{R}^3)$ be the function which we wish to reconstruct. The measured x-ray projections will be represented with the divergent beam (a.k.a. cone-beam) transform which is defined in 3-dimensions as

$$Df(\mathbf{y}, \boldsymbol{\theta}) = \int_0^\infty f(\mathbf{y} + \mathrm{t}\boldsymbol{\theta})\mathrm{dt}, \quad \mathbf{y} \in \mathbb{R}^3, \boldsymbol{\theta} \in S^2 = \text{unit sphere}.$$

The source curve is a helix, given by

$$\mathbf{y}(\mathrm{s}) = [\mathrm{R}\cos(\mathrm{s}), \mathrm{R}\sin(\mathrm{s}), \mathrm{P}\frac{\mathrm{s}}{2\pi}]^{\mathrm{T}}.$$

where R is the helical radius and P is the helical pitch (i.e. the displacement of the patient table per source turn). Also, denote the components of $\mathbf{x}$ as $\mathbf{x} = [\mathrm{x}_1, \mathrm{x}_2, \mathrm{x}_3]^{\mathrm{T}}$. Let U denote an open cylinder strictly inside the helix, i.e.

$$U = \{x \in \mathbb{R}^3 : x_1^2 + x_2^2 < r\}, \quad 0 < r < R.$$

Let Ω be the support of f. We will assume that $\Omega \subset U$.

A PI-line is any line segment that connects two points on the helix which are separated by less than one helical turn. For a helix of constant pitch, PI-lines satisfy a remarkable property: For every point $\mathbf{x}$ inside the helix, there is a unique PI-line which passes through $\mathbf{x}$. For a proof, see either [3] or [4]. Let $I_{PI} = [s_b, s_t]$ be the parametric interval corresponding to the unique PI-line passing through $\mathbf{x}$. In particular, $\mathbf{y}(s_b)$ and $\mathbf{y}(s_t)$ are the endpoints of the PI-line which lie on the helix. By definition, we have $s_t - s_b < 2\pi$. An illustration of a PI-line is in figure 2.1.

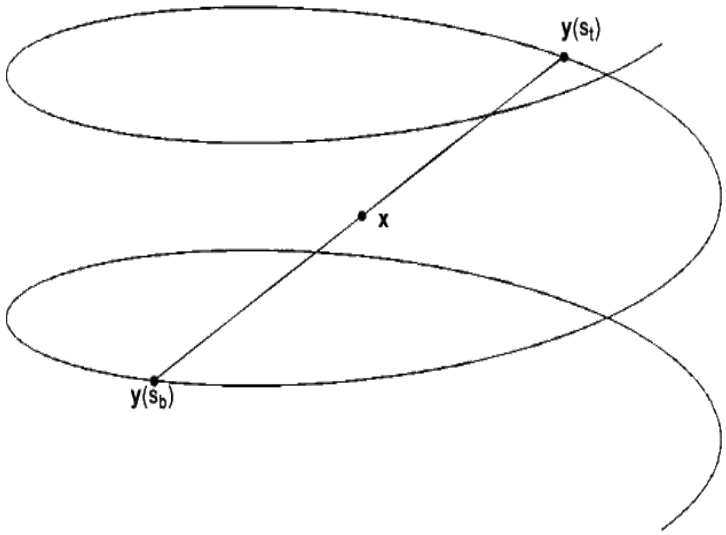

Figure 2.1: A PI-line

The region on the detector plane bounded above and below by the projections of the helix onto the detector plane when viewed from $\mathbf{y}(s)$ is called the Tam-Danielsson window in the literature (see figure 2.2). Now, consider the ray passing through $\mathbf{y}(s)$ and $\mathbf{x}$. Let the intersection of this ray with the detector plane be denoted by $\hat{\mathbf{x}}$. Tam et al.[17] and Danielsson et al. [3] showed that if $\hat{\mathbf{x}}$ lies inside the Tam-Danielsson window for every $s \in I_{PI}$, then $f(\mathbf{x})$ may be reconstructed exactly. For a given helical pitch, Noo et al. [15] used the Tam-Danielsson condition to derive formulas for the minimum detector size which allows for perfect reconstruction. Conversely, given a fixed detector size, these same formulas may be used to find the maximum pitch which allows for perfect reconstruction.

Following the terminology of Noo et al. [15], we define a κ-plane to be any plane that has three intersections with the helix such that one intersection is half-way between the two others. Denote the κ-plane which intersects the helix at the three points $\mathbf{y}(s)$, $\mathbf{y}(s+\psi)$, and $\mathbf{y}(s+2\psi)$ by $\kappa(s,\psi)$, where

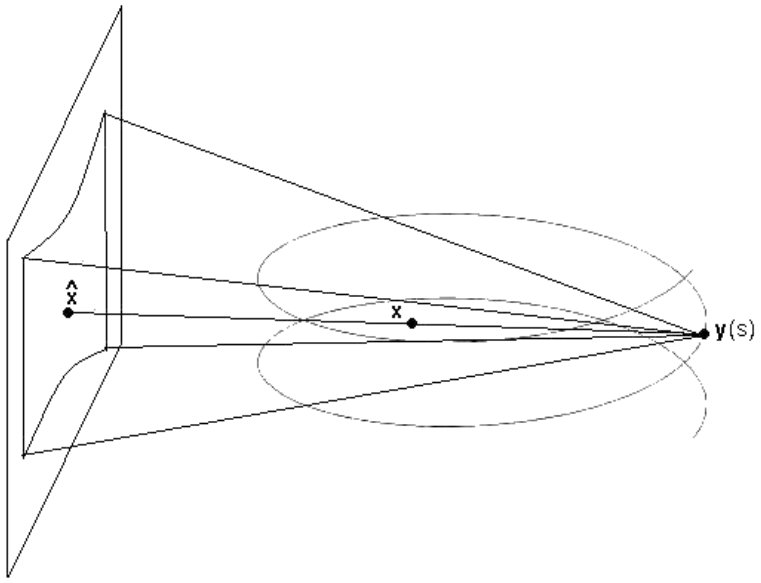

Figure 2.2: The Tam-Danielsson Window

$\psi \in (-\pi/2, \pi/2)$. Also, let the unit normal vector to $\kappa(s,\psi)$ be given by

$$\mathbf{n}(s,\psi) = \frac{(\mathbf{y}(s+\psi)-\mathbf{y}(s)) \times (\mathbf{y}(s+2\psi)-\mathbf{y}(s))}{\|((\mathbf{y}(s+\psi)-\mathbf{y}(s)) \times (\mathbf{y}(s+2\psi)-\mathbf{y}(s))\|}\text{sgn}(\psi), \quad \psi \in (-\pi/2, \pi/2).$$

Katsevich [12] proved that for a given $\mathbf{x}$, the κ-plane through $\mathbf{x}$ with $\psi \in (-\pi/2, \pi/2)$ is uniquely determined if the projection $\hat{\mathbf{x}}$ onto the detector plane lies in the Tam-Danielson window. Let a κ-line be the line of intersection of the detector plane and a κ-plane. So if $\hat{\mathbf{x}}$ lies in the Tam-Danielson window, there is a unique κ-line.

We will see that the Katsevich formula requires some data outside of the Tam-Danielson window. Therefore, we lose uniqueness of κ-lines. We will choose the κ-plane with smallest value of $|\psi|$ to use for the reconstruction. This condition is sufficient to ensure that we use the correct κ-lines.

Write the unit vector pointing from $\mathbf{y}(\mathrm{s})$ toward $\mathbf{x}$ as

$$\boldsymbol{\beta}(s,\mathbf{x}) = \frac{\mathbf{x}-\mathbf{y}(\mathrm{s})}{\|\mathbf{x}-\mathbf{y}(\mathrm{s})\|}.$$

Define $\mathbf{m}(s,\boldsymbol{\alpha})$ to be a unit normal vector for the plane $\kappa(s,\psi)$ with the smallest $|\psi|$ value that contains the line of direction $\boldsymbol{\alpha}$ which passes through $\mathbf{y}(s)$. Now, let $\mathbf{e}(s,\mathbf{x}) = \boldsymbol{\beta}(s,\mathbf{x}) \times \mathbf{m}(s,\boldsymbol{\beta})$. Here $\boldsymbol{\beta}(s,\mathbf{x})$ and $\mathbf{e}(s,\mathbf{x})$ span the κ-plane that we will want to use for the reconstruction. Any direction in this plane may be expressed by

$$\boldsymbol{\theta}(s,\mathbf{x},\gamma) = (\cos\gamma)\boldsymbol{\beta}(s,\mathbf{x}) + (\sin\gamma)\mathbf{e}(s,\mathbf{x}), \quad \gamma \in [0,2\pi).$$

2.2 The Inversion Formula

Now we are ready to state Katsevich's result.

Theorem 1 (Katsevich) *Let $f(\mathbf{x}) \in \mathrm{C}_0^\infty(\mathrm{U})$. Then*

$$f(\mathbf{x}) = -\frac{1}{2\pi^2}\int_{I_{PI}(\mathbf{x})} \frac{1}{\|\mathbf{x}-\mathbf{y}(s)\|} PV\int_0^{2\pi} \frac{\partial}{\partial q} Df(\mathbf{y}(q),\boldsymbol{\theta}(s,\mathbf{x},\gamma))\Big|_{q=s} \frac{d\gamma\, ds}{\sin\gamma}$$

where $I_{PI} = [s_b, s_t]$, $\boldsymbol{\theta}(s,\mathbf{x},\gamma) = (\cos\gamma)\boldsymbol{\beta}(s,\mathbf{x}) + (\sin\gamma)\mathbf{e}(s,\mathbf{x})$, $\mathbf{e}(s,\mathbf{x}) = \boldsymbol{\beta}(s,\mathbf{x}) \times \mathbf{m}(s,\boldsymbol{\beta})$, and $\mathbf{m}(s,\boldsymbol{\beta})$ is as defined in the previous section.

Proof:
See [10, 11, 12]. □

To see why Katsevich's formula is indeed of the filtered back-projection type, we rewrite it in three steps, similar to Noo et al. [15]. For fixed $\mathbf{x}$, consider the κ-plane with unit normal $\mathbf{m}(s,\boldsymbol{\beta}(s,\mathbf{x}))$. Let the unit vector $\boldsymbol{\eta}$ be the direction of any line in this plane. Since $\boldsymbol{\beta}(s,\mathbf{x})$ and $\mathbf{e}(\mathrm{s},\mathbf{x})$ span this plane, we may write $\boldsymbol{\eta}(s,\mathbf{x}) = (\cos\delta)\boldsymbol{\beta}(\mathrm{s},\mathbf{x}) + (\sin\delta)\mathbf{e}(s,\mathbf{x})$ for some $\delta \in [0,2\pi)$. Then define

$$g'(s,\boldsymbol{\eta}(s,\mathbf{x})) = \frac{\partial}{\partial q} Df(\mathbf{y}(q),\boldsymbol{\eta}(s,\mathbf{x}))\Big|_{q=s}$$

and

$$g^F(s,\boldsymbol{\eta}(s,\mathbf{x})) = PV\int_0^{2\pi} k_H(\sin\gamma)\, g'(s,\cos(\delta-\gamma)\boldsymbol{\beta}(s,\mathbf{x}) - \sin(\delta-\gamma)\mathbf{e}(s,\mathbf{x}))\, d\gamma.$$

So that the Katsevich formula takes the form

$$f(\mathbf{x}) = -\frac{1}{2\pi}\int_{\mathrm{I_{PI}(x)}} \frac{1}{\|\mathbf{x}-\mathbf{y}(s)\|}\mathrm{g^F(s,\boldsymbol{\beta}(s,x))}\,ds.$$

Therefore, we see that Katsevich's formula may be implemented as a derivative, followed by a 1-D convolution, and then a back-projection. In particular, the filtering resembles a modified Hilbert transform. We will see in chapter 3 that the filter may be implemented using regular 1-D Hilbert transforms.

The FBP algorithm for 2-D parallel beam CT may be viewed as an implementation of an inversion formula which consists of a derivative, a Hilbert transform, and then a back-projection (e.g. see [13]). It is interesting to see that Katsevich's inversion formula consists of the same operations, although modified.

We now state a generalization of Katsevich's formula due to Ye and Wang [20]. Their theorem applies to more general scanning curves and also relaxes the smoothness requirement on $f(\mathbf{x})$.

Theorem 2 (Generalized Katsevich Formula) *Let $f(\mathbf{x}) \in \mathrm{C_0^5}(\mathbb{R}^3)$ and let $\mathbf{y}(\mathrm{s})$ be a bounded, smooth curve for $s_b \le s \le s_t$ which lies outside of $\Omega = supp\ f(\mathbf{x})$. Let $\mathbf{x}$ be an interior point on the chord which connect the endpoints $\mathbf{y}(\mathrm{s_b})$ and $\mathbf{y}(\mathrm{s_t})$. Also, let $\mathbf{e}(\mathrm{s},\mathbf{x})$ be a unit vector perpendicular to $\boldsymbol{\beta}(s,\mathbf{x})$. Define the set*

$$S(\mathbf{x},\boldsymbol{\nu}) = \{s \in [s_b, s_t] \ : \ < \boldsymbol{\nu}, \mathbf{x}-\mathbf{y}(\mathrm{s}) >= 0\}.$$

Assume that $\forall s, \mathbf{y}'(s) \times \mathbf{y}''(s) \neq 0$. Also, assume that S is nonempty and finite for almost all $\boldsymbol{\nu} \in \mathbb{R}^3$ and that $\mathbf{e}(\mathrm{s},\mathbf{x})$ satisfies the admissibility condition

$$\sum_{s_j \in S} \mathrm{sgn}(< \boldsymbol{\nu}, \mathbf{y}'(\mathrm{s_j}) >)\mathrm{sgn}(< \boldsymbol{\nu}, \mathbf{e}(\mathrm{s_j},\mathbf{x}) >) = 1 \quad \text{for almost all } \boldsymbol{\nu} \in \mathbb{R}^3.$$

Then

$$f(\mathbf{x}) = -\frac{1}{2\pi^2}\int_{\mathrm{s_b}}^{\mathrm{s_t}} \frac{1}{\|\mathbf{x}-\mathbf{y}(s)\|}\mathrm{PV}\int_0^{2\pi} \frac{\partial}{\partial \mathrm{q}}\mathrm{Df}(\mathbf{y}(q),\boldsymbol{\theta}(s,\mathbf{x},\gamma))\Big|_{q=s}\frac{d\gamma\, ds}{\sin\gamma}.$$

Some of the hypotheses for the above theorem are not stated clearly by Ye and Wang, but are assumed in their proof.

In 1983, Tuy [18] derived an inversion formula for cone-beam tomography which imposed a similar condition on the source curve. Let $\mathbf{y}(\lambda)$ with $\lambda \in \Lambda$ be a smooth and bounded source curve, which lies outside of Ω. Then Tuy's condition is

$$\forall(\mathbf{x}, \boldsymbol{\nu}) \in \Omega \times \mathrm{S}^2, \exists \lambda \in \Lambda \text{ such that } < \boldsymbol{\nu}, \mathbf{x} - \mathbf{y}(\lambda) >= 0 \text{ and } < \mathbf{y}'(\lambda), \boldsymbol{\nu} > \neq 0.$$

This condition may be interpreted geometrically as follows: For any point $\mathbf{x} \in \Omega$ and any direction $\boldsymbol{\nu}$, the plane orthogonal to $\boldsymbol{\nu}$ containing $\mathbf{x}$ must intersect the source curve at some point $\mathbf{y}(\lambda)$ for which $< \mathbf{y}'(\lambda), \boldsymbol{\nu} > \neq 0$. Chen [2] and Zhao et al. [21] impose conditions on the source curve similar to the above theorem and comment on their relation to Tuy's conditions.

Chapter 3

Implementation for a Flat Detector

In this chapter, we will consider implementation of Katsevich's formula for a flat detector. The curved detector case is considered in the next chapter. We will mainly follow the implementation suggested by Noo, Pack and Heuscher in [15]. Additional details that are not presented in [15] will also be provided.

3.1 Flat Detector Geometry

The source curve is a helix, given by

$$\mathbf{y}(\mathrm{s}) = [\mathrm{R}\cos(\mathrm{s}), \mathrm{R}\sin(\mathrm{s}), \mathrm{P}\frac{\mathrm{s}}{2\pi}]^{\mathrm{T}}.$$

where R is the helical radius and P is the helical pitch (i.e. the displacement of the patient table per source turn). For convenience, let $h = P/(2\pi)$. Also, let D be the source to detector distance. For a flat detector, introduce the local detector coordinates (u, v, w) with unit vectors

$$\mathbf{e}_{\mathrm{u}}(\mathrm{s}) = [-\sin(\mathrm{s}), \cos(\mathrm{s}), 0]^{\mathrm{T}}$$

$$\mathbf{e}_{\mathrm{v}}(\mathrm{s}) = [-\cos(\mathrm{s}), -\sin(\mathrm{s}), 0]^{\mathrm{T}}$$

$$\mathbf{e}_{\mathrm{w}} = [0, 0, 1]^{\mathrm{T}}.$$

Here $\mathbf{e}_{\mathrm{v}}(\mathrm{s})$ points from the source point $\mathbf{y}(\mathrm{s})$ to the center of the detector, and the unit vectors $\mathbf{e}_{\mathrm{u}}(\mathrm{s})$ and $\mathbf{e}_{\mathrm{w}}$ span the detector.

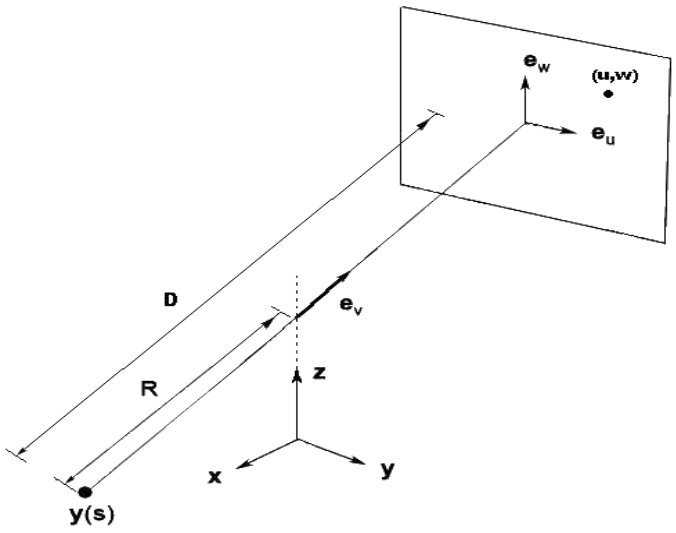

Figure 3.1: Flat Detector Geometry

Given (s, u, w), we may express the x-ray projection data with these local coordinates as

$$g_f(s, u, w) = Df(\mathbf{y}(\mathrm{s}), \boldsymbol{\theta}_f)$$

where the subscript "f" means that the data is for a flat detector. In the above formula,

$$\boldsymbol{\theta}_f(s, u, w) = \frac{1}{\sqrt{u^2 + D^2 + w^2}}(u\mathbf{e}_{\mathrm{u}}(\mathrm{s}) + \mathrm{D}\mathbf{e}_{\mathrm{v}}(\mathrm{s}) + \mathrm{w}\mathbf{e}_{\mathrm{w}}) \tag{3.1}$$

is a unit vector in the direction of the ray which passes through $\mathbf{y}(\mathrm{s})$ and which intersects the detector at coordinates (u, w).

On the other hand, given $(s, \boldsymbol{\theta})$, we can also express the projection data in terms of detector coordinates. To see how, orthogonally project the line with source point $\mathbf{y}(\mathrm{s})$ and direction $\boldsymbol{\theta}$ onto the plane $z = hs$. Then let α be the angle between this projection and $\mathbf{e}_{\mathrm{v}}$. The desired u-coordinate is

$$u_f = D\tan\alpha = D\frac{< \boldsymbol{\theta}, \mathbf{e}_{\mathrm{u}}(\mathrm{s}) >}{< \boldsymbol{\theta}, \mathbf{e}_{\mathrm{v}}(\mathrm{s}) >}. \tag{3.2}$$

In a similar fashion, one may show that

$$w_f = D\frac{< \boldsymbol{\theta}, \mathbf{e}_{\mathrm{w}} >}{< \boldsymbol{\theta}, \mathbf{e}_{\mathrm{v}}(\mathrm{s}) >}. \tag{3.3}$$

Hence, (u_f, w_f) are the local coordinates of the intersection of the line with direction $\boldsymbol{\theta}$ and source point $\mathbf{y}(\mathrm{s})$ with the detector, and we may write

$$Df(\mathbf{y}(\mathrm{s}), \boldsymbol{\theta}) = g_f(s, u_f, w_f).$$

Write the unit vector pointing from $\mathbf{y}(\mathrm{s})$ toward $\mathbf{x}$ as

$$\boldsymbol{\beta}(s, \mathbf{x}) = \frac{\mathbf{x} - \mathbf{y}(\mathrm{s})}{\|\mathbf{x} - \mathbf{y}(\mathrm{s})\|}.$$

Then it follows from the above formulas that

$$Df(\mathbf{y}(\mathrm{s}), \boldsymbol{\beta}) = g_f(s, u^*, w^*),$$

where

$$v^*(s, \mathbf{x}) = \mathrm{R} - \mathrm{x}_1 \cos(\mathrm{s}) - \mathrm{x}_2 \sin(\mathrm{s}) = \mathrm{R} + < \mathbf{x}, \mathbf{e}_v >,$$

$$\begin{aligned} u^*(s, \mathbf{x}) &= D\frac{< \boldsymbol{\beta}, \mathbf{e}_{\mathrm{u}} >}{< \boldsymbol{\beta}, \mathbf{e}_{\mathrm{v}} >} \\ &= D\frac{< \mathbf{x} - \mathbf{y}, \mathbf{e}_{\mathrm{u}} >}{< \mathbf{x} - \mathbf{y}, \mathbf{e}_{\mathrm{v}} >} \\ &= D\frac{< \mathbf{x}, \mathbf{e}_{\mathrm{u}} >}{R + < \mathbf{x}, \mathbf{e}_{\mathrm{v}} >} \\ &= \frac{D}{v^*(s, x)}(-x_1 \sin(s) + x_2 \cos(s)), \end{aligned}$$

and

$$\begin{aligned} w^*(s, \mathbf{x}) &= D\frac{< \boldsymbol{\beta}, \mathbf{e}_{\mathrm{w}} >}{< \boldsymbol{\beta}, \mathbf{e}_{\mathrm{v}} >} \\ &= D\frac{< \mathbf{x} - \mathbf{y}, \mathbf{e}_{\mathrm{w}} >}{< \mathbf{x} - \mathbf{y}, \mathbf{e}_{\mathrm{v}} >} \\ &= D\frac{z - hs}{R + < \mathbf{x}, \mathbf{e}_{\mathrm{v}} >} \\ &= \frac{D}{v^*(s, x)}(x_3 - hs). \end{aligned}$$

Here (u^*, w^*) are the coordinates for the point of intersection of the detector with the line passing through $y(s)$ and $\mathbf{x}$. Moreover, note that $< \mathbf{x}, -\mathbf{e}_{\mathrm{v}} > (-\mathbf{e}_{\mathrm{v}})$ is the projection of $\mathbf{x}$ onto the line from the center of the detector to $\mathbf{y}(\mathrm{s})$. Then $v^* = R - < \mathbf{x}, -\mathbf{e}_{\mathrm{v}} >$ is the distance from $\mathbf{y}(\mathrm{s})$ to this projection.

3.2 The Katsevich Formula in Local Flat Detector Coordinates

In this section, we will express the Katsevich formula in the local flat detector coordinates. First, we must find the equation for the κ-line of angle ψ. Recall that this line is the intersection of the κ-plane, $\kappa(s, \psi)$, with the detector plane.

Lemma 1 *Let $\psi \in (-\pi/2, \pi/2)$. The equation for the κ-line of angle ψ is*

$$w_\kappa = \frac{DP}{2\pi R}\left(\psi + \frac{\psi}{D\tan\psi}u\right).$$

Proof:

We will first solve for two points (u_1, w_1) and (u_2, w_2) on the κ-line. The plane $\kappa(s, \psi)$ contains the points $\mathbf{y}(s)$, $\mathbf{y}(s+\psi)$, and $\mathbf{y}(s+2\psi)$. Let (u_1, w_1) be the intersection of the detector plane with the line through $\mathbf{y}(\mathrm{s})$ and $\mathbf{y}(\mathrm{s}+\psi)$. Similarly, let (u_2, w_2) be the intersection of the detector with the line through $\mathbf{y}(s)$ and $\mathbf{y}(s+2\psi)$.

Using the definition for the helix, $\mathbf{y}(\mathrm{s})$,we have

$$\mathbf{y}(\mathrm{s}) = [\mathrm{R}\cos(\mathrm{s}), \mathrm{R}\sin(\mathrm{s}), \mathrm{P}\frac{\mathrm{s}}{2\pi}]^{\mathrm{T}}$$

and

$$\mathbf{y}(\mathrm{s}+\psi) = [\mathrm{R}\cos(\mathrm{s}+\psi), \mathrm{R}\sin(\mathrm{s}+\psi), \frac{\mathrm{P}}{2\pi}(\mathrm{s}+\psi)]^{\mathrm{T}}.$$

Since $\cos(s+\psi) = \cos s\cos\psi - \sin s\sin\psi$ and $\sin(s+\psi) = \sin s\cos\psi + \cos s\sin\psi$,

$$\mathbf{y}(\mathrm{s}+\psi) - \mathbf{y}(\mathrm{s}) = \begin{bmatrix} R(\cos s\cos\psi - \sin s\sin\psi - \cos s) \\ R(\sin s\cos\psi + \cos s\sin\psi - \sin s) \\ \frac{P}{2\pi}\psi \end{bmatrix}.$$

Combining this with the definitions of the unit vectors $\mathbf{e}_{\mathrm{u}}$, $\mathbf{e}_{\mathrm{v}}$, and $\mathbf{e}_{\mathrm{w}}$ yields

$$\mathbf{y}(\mathrm{s}+\psi)-\mathbf{y}(\mathrm{s}) = \mathrm{R}\sin\psi\ \mathbf{e}_{\mathrm{u}}(\mathrm{s}) + \mathrm{R}(1-\cos\psi)\ \mathbf{e}_{\mathrm{v}}(\mathrm{s}) + \frac{\mathrm{P}}{2\pi}\psi\ \mathbf{e}_{\mathrm{w}}(\mathrm{s}).$$

Now using the equations for u_f and w_f with $\boldsymbol{\theta} = \mathbf{y}(\mathrm{s}+\psi)-\mathbf{y}(\mathrm{s})$ we find that

$$u_1 = D\frac{\sin\psi}{1-\cos\psi}, \qquad w_1 = \frac{DP}{2\pi R}\ \frac{\psi}{1-\cos\psi}.$$

In order to find (u_2, w_2) we simply replace ψ with 2ψ in the above derivation to get

$$u_1 = D\frac{\sin(2\psi)}{1-\cos(2\psi)}, \qquad w_1 = \frac{DP}{2\pi R}\ \frac{2\psi}{1-\cos(2\psi)}.$$

Next, we find the slope of the line through (u_1, w_1) and (u_2, w_2).

$$\begin{aligned}
m &= \frac{w_2-w_1}{u_2-u_1} \\
&= \frac{\frac{DP}{2\pi R}\left[\frac{2\psi}{1-\cos(2\psi)} - \frac{\psi}{1-\cos\psi}\right]}{D\left[\frac{\sin(2\psi)}{1-\cos(2\psi)} - \frac{\sin\psi}{1-\cos\psi}\right]} \\
&= \frac{DP}{2\pi R}\frac{1}{D}\left[\frac{\frac{2\psi(1-\cos\psi)-\psi(1-\cos(2\psi))}{(1-\cos(2\psi))(1-\cos\psi)}}{\frac{\sin(2\psi)(1-\cos\psi)-\sin\psi(1-\cos(2\psi))}{(1-\cos(2\psi))(1-\cos\psi)}}\right] \\
&= \frac{DP}{2\pi R}\frac{1}{D}\left[\frac{2\psi-2\psi\cos\psi-\psi+\psi\cos(2\psi)}{\sin(2\psi)-\sin(2\psi)\cos\psi-\sin\psi+\sin\psi\cos(2\psi)}\right] \\
&= \frac{DP}{2\pi R}\frac{1}{D}\left[\frac{\psi(1-2\cos\psi+\cos(2\psi))}{2\sin\psi\cos\psi-2\sin\psi\cos^2\psi-\sin\psi+\sin\psi(2\cos^2\psi-1)}\right] \\
&= \frac{DP}{2\pi R}\frac{1}{D}\left[\frac{\psi(1-2\cos\psi+2\cos^2\psi-1)}{2\sin\psi\cos\psi-2\sin\psi}\right] \\
&= \frac{DP}{2\pi R}\frac{1}{D}\left[\frac{2\psi\cos\psi(\cos\psi-1)}{2\sin\psi(\cos\psi-1)}\right] \\
&= \frac{DP}{2\pi R}\frac{1}{D}\frac{\psi}{\tan\psi}
\end{aligned}$$

Therefore, the equation for the κ-line is

$$\begin{aligned} w_\kappa &= w_1 + m(u - u_1) \\ &= \frac{DP}{2\pi R}\left[\frac{\psi}{1-\cos\psi} + \frac{\psi}{D\tan\psi}\left(u - \frac{D\sin\psi}{1-\cos\psi}\right)\right] \\ &= \frac{DP}{2\pi R}\left[\frac{\psi}{1-\cos\psi} + \frac{\psi}{D\tan\psi}u - \frac{\psi\sin\psi}{\tan\psi(1-\cos\psi)}\right], \end{aligned}$$

which further simplifies to

$$\begin{aligned} w_\kappa &= \frac{DP}{2\pi R}\left[\frac{\psi}{1-\cos\psi} - \frac{\psi\cos\psi}{1-\cos\psi} + \frac{\psi}{D\tan\psi}u\right] \\ &= \frac{DP}{2\pi R}\left[\frac{\psi(1-\cos\psi)}{1-\cos\psi} + \frac{\psi}{D\tan\psi}u\right] \\ &= \frac{DP}{2\pi R}\left[\psi + \frac{\psi}{D\tan\psi}u\right]. \end{aligned}$$

□

Examining figure 3.2, we see that some κ-lines pass outside of the Tam-Danielsson window. All of the data on these κ-lines are necessary for the filtering step of the Katsevich formula. Therefore, the Katsevich formula requires some data outside of the Tam-Danielson window. Let r be the field of view radius. Katsevich [12, p.694] comments that as $r/R \to 1$, the amount of data in excess of the Tam-Danielsson window required for the reconstruction increases, but slowly.

Recall from chapter 2, that Katsevich's formula may be rewritten using the definitions

$$g'(s, \boldsymbol{\eta}(s,\mathbf{x})) = \frac{\partial}{\partial q} Df(\mathbf{y}(q), \boldsymbol{\eta}(s,\mathbf{x}))\Big|_{q=s}$$

and

$$g^F(s,\boldsymbol{\eta}(s,\mathbf{x})) = PV\int_0^{2\pi} k_H(\sin\gamma)\, g'(s, \cos(\delta-\gamma)\boldsymbol{\beta}(s,\mathbf{x}) - \sin(\delta-\gamma)\mathbf{e}(s,\mathbf{x}))\, d\gamma,$$

where $\boldsymbol{\eta}(s,\mathbf{x}) = (\cos\delta)\boldsymbol{\beta}(\mathrm{s},\mathbf{x}) + (\sin\delta)\mathbf{e}(s,\mathbf{x})$ for some $\delta \in [0, 2\pi)$. Note that $\boldsymbol{\eta}$ is independent of q in the derivative formula. Then the Katsevich formula takes the form

$$f(\mathbf{x}) = -\frac{1}{2\pi}\int_{\mathrm{I_{PI}}(\mathbf{x})} \frac{1}{\|\mathbf{x}-\mathbf{y}(s)\|} g^F(s, \boldsymbol{\beta}(s,\mathbf{x}))\, ds.$$

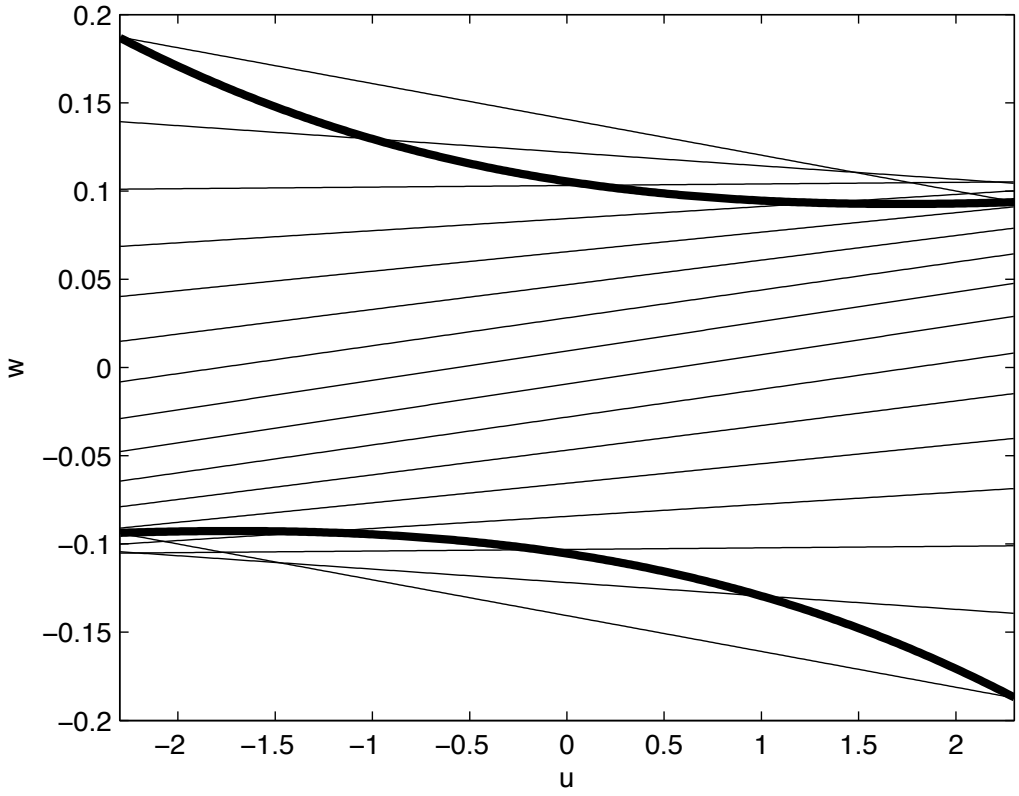

Figure 3.2: κ-lines on a Flat Detector, The dark curves are the edges of the Tam-Danielsson window.

Next, we will write these formulas in terms of detector coordinates.

Recall that $g_f(s,u,w) = Df(\mathbf{y}(\mathrm{s}), \boldsymbol{\theta}_f)$, where $\boldsymbol{\theta}_f(s,u,w)$ is a unit vector in the direction of the line which contains $\mathbf{y}(\mathrm{s})$ and intersects the detector at (u,w). We define

$$g_1(s,u,w) := g'(s, \boldsymbol{\theta}_f(s,u,w)) = \frac{\partial}{\partial q} Df(\mathbf{y}(q), \boldsymbol{\theta}_f(s,u,w))\Big|_{q=s} = \frac{\partial}{\partial q} g_f(q,u,w)\Big|_{q=s}$$

and have the following lemma.

Lemma 2

$$g_1(s,u,w) = (\frac{\partial g_f}{\partial q} + \frac{u^2+D^2}{D}\frac{\partial g_f}{\partial u} + \frac{uw}{D}\frac{\partial g_f}{\partial w})\Big|_{q=s}$$

Proof:
Using the chain rule, we have

$$g_1(s,u,w) = \frac{\partial}{\partial q} g_f(q,u,w)\Big|_{q=s} = (\frac{\partial g_f}{\partial q} + \frac{\partial g_f}{\partial u}\frac{\partial u}{\partial q} + \frac{\partial g_f}{\partial w}\frac{\partial w}{\partial q})\Big|_{q=s}.$$

Recall that

$$\boldsymbol{\theta}_f(s,u,w) = \frac{1}{\sqrt{u^2+D^2+w^2}}(u\mathbf{e}_{\mathrm{u}}(\mathrm{s}) + \mathrm{D}\mathbf{e}_{\mathrm{v}}(\mathrm{s}) + \mathrm{w}\mathbf{e}_{\mathrm{w}}).$$

The ray with source point $\mathbf{y}(s)$ and direction $\boldsymbol{\theta}_f(s,u,w)$ intersects the detector at (u,w). From equations (3.2) and (3.3),

$$u = D\frac{<\boldsymbol{\theta}_f, \mathbf{e}_{\mathrm{u}}(\mathrm{q})>}{<\boldsymbol{\theta}_f, \mathbf{e}_{\mathrm{v}}(\mathrm{q})>} \qquad \text{and} \qquad w = D\frac{<\boldsymbol{\theta}_f, \mathbf{e}_{\mathrm{w}}>}{<\boldsymbol{\theta}_f, \mathbf{e}_{\mathrm{v}}(\mathrm{q})>}.$$

Using the quotient rule and the facts that $\mathbf{e}'_{\mathrm{u}} = \mathbf{e}_{\mathrm{v}}$, $\mathbf{e}'_{\mathrm{v}} = -\mathbf{e}_{\mathrm{u}}$ and $\mathbf{e}'_{\mathrm{w}}$=0, we find that

$$\begin{aligned}
\frac{\partial u}{\partial q} &= D\frac{<\boldsymbol{\theta}_f, \mathbf{e}'_{\mathrm{u}}><\boldsymbol{\theta}_f, \mathbf{e}_{\mathrm{v}}> - <\boldsymbol{\theta}_f, \mathbf{e}_{\mathrm{u}}><\boldsymbol{\theta}_f, \mathbf{e}'_{\mathrm{v}}>}{<\boldsymbol{\theta}_f, \mathbf{e}_{\mathrm{v}}>^2} \\
&= D\frac{<\boldsymbol{\theta}_f, \mathbf{e}_{\mathrm{v}}>^2 + <\boldsymbol{\theta}_f, \mathbf{e}_{\mathrm{u}}>^2}{<\boldsymbol{\theta}_f, \mathbf{e}_{\mathrm{v}}>^2} \\
&= D\frac{D^2+u^2}{D^2} \\
&= \frac{u^2+D^2}{D}
\end{aligned}$$

and

$$\begin{aligned}
\frac{\partial w}{\partial q} &= D\frac{<\boldsymbol{\theta}_f, \mathbf{e}'_{\mathrm{w}}><\boldsymbol{\theta}_f, \mathbf{e}_{\mathrm{v}}> - <\boldsymbol{\theta}_f, \mathbf{e}_{\mathrm{w}}><\boldsymbol{\theta}_f, \mathbf{e}'_{\mathrm{v}}>}{<\boldsymbol{\theta}_f, \mathbf{e}_{\mathrm{v}}>^2} \\
&= D\frac{<\boldsymbol{\theta}_f, \mathbf{e}_{\mathrm{w}}><\boldsymbol{\theta}_f, \mathbf{e}_{\mathrm{u}}>}{<\boldsymbol{\theta}_f, \mathbf{e}_{\mathrm{v}}>^2} \\
&= D\frac{wu}{D^2} \\
&= \frac{uw}{D}.
\end{aligned}$$

Then g_1 simplifies to

$$g_1(s,u,w) = (\frac{\partial g_f}{\partial q} + \frac{u^2+D^2}{D}\frac{\partial g_f}{\partial u} + \frac{uw}{D}\frac{\partial g_f}{\partial w})\Big|_{q=s}.$$

□

For $\gamma \in [0, 2\pi)$, consider the line of direction $\boldsymbol{\theta}(s, \mathbf{x}, \gamma) = (\cos\gamma)\boldsymbol{\beta}(s, \mathbf{x}) + (\sin\gamma)\mathbf{e}(s, \mathbf{x})$ which passes through the source point $\mathbf{y}(\mathrm{s})$. As γ varies, the line sweeps out the κ-plane with unit normal $\mathbf{m}(\mathrm{s}, \boldsymbol{\beta})$. Therefore, the intersection of this line with the detector plane sweeps out a κ-line as γ varies. Denote this intersection by (u', w'_κ). Also let (u, w_κ) be the intersection of the detector plane with the line passing through $\mathbf{y}(\mathrm{s})$ with direction $\boldsymbol{\beta}(s, \mathbf{x})$. See figure 3.3 for an illustration. Next, we prove a lemma which expresses the convolution in detector coordinates.

Lemma 3 *Let* $r = \sqrt{u^2 + D^2 + w_\kappa^2}$ *and* $r' = \sqrt{(u')^2 + D^2 + (w'_\kappa)^2}$ *be the distances from* $\mathbf{y}(\mathrm{s})$ *to the detector points* $(u, w_\kappa(u))$ *and* $(u', w'_\kappa(u'))$*, respectively. Then*

$$g^F(s, \boldsymbol{\beta}) = -\frac{r}{D}\int_{-\infty}^{\infty} k_H(u-u')\frac{D}{r'}g_1(s, u', w'_\kappa)du'.$$

Proof:

Refer to the labels of Figure 3.3. Using the Law of Sines,

$$\frac{L}{\sin\gamma} = \frac{r'}{l/r} \qquad \Rightarrow \qquad lL = rr'\sin\gamma$$

and

$$\frac{\Delta L}{\sin(\Delta\gamma)} = \frac{r'}{l/r''} \qquad \Rightarrow \qquad l\Delta L = r'r''\sin(\Delta\gamma).$$

Dividing these two equations yields

$$\frac{\Delta L}{L} = \frac{r''\sin\Delta\gamma}{r\sin\gamma}, \quad \gamma \neq 0. \tag{3.4}$$

Next, we see that

$$\sin\lambda = \frac{u'-u}{L} = \frac{\Delta u}{\Delta L}.$$

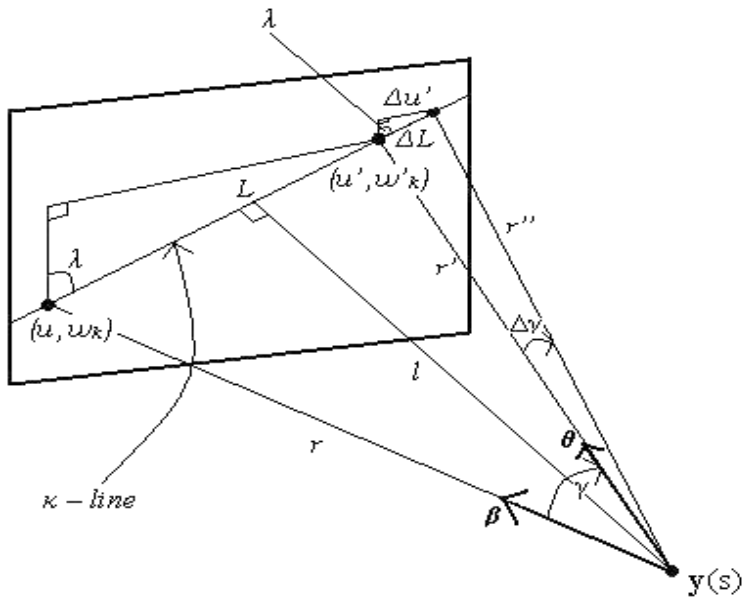

Figure 3.3: Relation between γ and the flat detector coordinates.

Hence,

$$\frac{\Delta L}{L} = \frac{\Delta u'}{u' - u}.$$

Combining with equation (3.4) gives

$$\frac{\Delta u'}{u' - u} = \frac{r'' \sin \Delta\gamma}{r \sin \gamma}, \quad \gamma \neq 0.$$

Letting $\Delta\gamma$ become infinitesimal, the last equation becomes

$$\frac{du'}{u' - u} = \frac{r' d\gamma}{r \sin \gamma}, \quad \gamma \neq 0.$$

Written another way, we have

$$k_H(\sin\gamma)d\gamma = -\frac{r}{r'}k_H(u-u')du', \quad \gamma \neq 0.$$

Recall that

$$g^F(s,\boldsymbol{\beta}) = PV\int_0^{2\pi} k_H(\sin\gamma)g'(s,\cos(\gamma)\boldsymbol{\beta}(s,\mathbf{x}) + \sin(\gamma)\mathbf{e}(s,\mathbf{x}))d\gamma.$$

We may now write this as an integral in u' using the relation between differentials derived above. Note that the integral in γ occurs over the κ-line $w'_\kappa(\psi,u')$, where ψ is chosen to have the smallest $|\psi|$ such that the κ-plane contains the line of direction $\boldsymbol{\beta}$ which passes through $\mathbf{y}$(s). Also, note that the data is zero for $\gamma \notin (-\pi/2,\pi/2)$ because those rays do not intersect the region of interest. Hence,

$$g^F(s,\boldsymbol{\beta}) = -\frac{r}{D}\int_{-\infty}^{\infty} k_H(u-u')\frac{D}{r'}g_1(s,u',w'_\kappa)du'.$$

□

Lemma 4 *Let*

$$g_f^F(s,u,w_\kappa) := \int_{-\infty}^{\infty} k_H(u-u')\frac{D}{\sqrt{(u')^2+D^2+(w'_\kappa)^2}}g_1(s,u',w'_\kappa)du'.$$

Then

$$\frac{-1}{\|\mathbf{x}-\mathbf{y}(s)\|}g^F(s,\boldsymbol{\beta}) = \frac{1}{v^*(s,\mathbf{x})}g_f^F(s,u,w_\kappa)$$

Proof:
Let $r = \sqrt{u^2+D^2+w_\kappa^2}$. From Lemma 3 we see that

$$g^F(s,\boldsymbol{\beta}) = -\frac{r}{D}g_f^F(s,u,w_\kappa).$$

Refer to Figures 3.1 and 3.3. By similar triangles (not drawn on Figure 3.3),

$$\frac{r}{D} = \frac{\|\mathbf{x}-\mathbf{y}(s)\|}{<(\mathbf{x}-\mathbf{y}(s)),\mathbf{e}_v>} \qquad \Rightarrow \qquad \frac{r}{D\|\mathbf{x}-\mathbf{y}(s)\|} = \frac{1}{<(\mathbf{x}-\mathbf{y}(s)),\mathbf{e}_v>}.$$

As a consequence, we have

$$\begin{aligned}\frac{-1}{\|\mathbf{x}-\mathbf{y}(s)\|}g^F(s,\boldsymbol{\beta}) &= \frac{1}{\|\mathbf{x}-\mathbf{y}(s)\|}\frac{r}{D}g_f^F(s,u,w_\kappa)\\ &= \frac{1}{<(\mathbf{x}-\mathbf{y}(s)),\mathbf{e}_v>}g_f^F(s,u,w_\kappa)\\ &= \frac{1}{(R+<\mathbf{x},\mathbf{e}_{\mathrm{v}}>)}g_f^F(s,u,w_\kappa)\\ &= \frac{1}{v^*(s,\mathbf{x})}g_f^F(s,u,w_\kappa).\square\end{aligned}$$

Recall that the line passing through $\mathbf{y}$(s) with direction $\boldsymbol{\beta}$ intersects the detector at (u^*,w^*). Collecting our results, we have proven the following theorem.

Theorem 3 (Katsevich formula in local flat detector coordinates) *Let* $g_f(s,u,w) := Df(\mathbf{y}(s),\boldsymbol{\theta}_f)$, *where*

$$\boldsymbol{\theta}_f(s,u,w) = \frac{1}{\sqrt{u^2+D^2+w^2}}(u\mathbf{e}_u(s)+D\mathbf{e}_v(s)+w\mathbf{e}_{\mathrm{w}}).$$

Also, let v^*, u^*, *and* w^* *be given by*

$$v^*(s,\mathbf{x}) = R - x_1\cos(s) - x_2\sin(s),$$

$$u^*(s,\mathbf{x}) = \frac{D}{v^*(s,\mathbf{x})}(-x_1\sin(s)+x_2\cos(s)),$$

and

$$w^*(s,\mathbf{x}) = \frac{D}{v^*(s,\mathbf{x})}(x_3 - hs).$$

Then the Katsevich formula may be written in local coordinates for a flat detector with the equations

$$g_1(s,u,w) = \left(\frac{\partial g_f(q,u,w)}{\partial q} + \frac{u^2+D^2}{D}\frac{\partial g_f(q,u,w)}{\partial u} + \frac{uw}{D}\frac{\partial g_f(q,u,w)}{\partial w}\right)\Big|_{q=s},$$

$$g_f^F(s,u,w_\kappa) := \int_{-\infty}^{\infty} k_H(u-u')\frac{D}{\sqrt{(u')^2+D^2+(w'_\kappa)^2}}g_1(s,u',w'_\kappa)du',$$

and

$$f(\mathbf{x}) = \frac{1}{2\pi}\int_{\mathrm{I_{PI}(x)}}\frac{1}{v^*(s,\mathbf{x})}\mathrm{g}_f^F(s,u^*,w^*)ds.$$

3.3 PI-lines

In order to implement the back-projection, we must find an expression for the PI-line intervals. Kyle Champley [1] has discovered an exact non-linear equation which may be used to solve for s_b, and consequently, s_t. The derivation in [1] is followed below, but with some additional details provided.

Lemma 5 *For any fixed* $\mathbf{x} = [\mathrm{x}_1, \mathrm{x}_2, \mathrm{x}_3]^{\mathrm{T}} \in \Omega \subset \mathrm{U}$, *write* $\mathbf{x}$ *in cylindrical coordinates as* $\mathbf{x} = [r\cos\gamma, r\sin\gamma, x_3]^T$. *Let* $\mathbf{y}(s_t)$ *and* $\mathbf{y}(s_b)$ *denote the top and bottom of the PI-line segment for* $\mathbf{x}$, *so that the parametric interval is* $I_{PI(\mathbf{x})} = [s_b, s_t]$. *Then* s_b *satisfies*

$$x_3 = h\left[\left(\pi - 2\arctan\left(\frac{r\sin(\gamma - s_b)}{R - r\cos(\gamma - s_b)}\right)\right) \times \left(1 + \frac{r^2 - R^2}{2R(R - r\cos(\gamma - s_b))}\right) + s_b\right]$$

where

$$\frac{x_3}{h} - 2\pi \leq s_b \leq \frac{x_3}{h}.$$

In addition, $s_t = s_b + \pi - 2\alpha$ *with*

$$\alpha = \arctan\left(\frac{r\sin(\gamma - s_b)}{R - r\cos(\gamma - s_b)}\right).$$

Proof:

Let $\hat{\mathbf{x}}$ be the orthogonal projection of $\mathbf{x}$ onto the x_1-x_2 plane. Consider any chord which passes through $\hat{\mathbf{x}}$ with endpoints on the circle of radius R in the x_1-x_2 plane. Note that there are an infinite number of such chords. First, we will try to relate the endpoints of such a chord. For each $\beta \in [0, 2\pi)$, there is a unique $\beta' \in [0, 2\pi)$ such that the chord connecting $\hat{\mathbf{y}}(\beta) = [R\cos\beta, R\sin\beta]^T$ and $\hat{\mathbf{y}}(\beta') = [R\cos\beta', R\sin\beta']^T$ intersects $\hat{\mathbf{x}}$.

The vector from $\hat{\mathbf{x}}$ to $\hat{\mathbf{y}}(\beta)$ is given by

$$\overrightarrow{\hat{\mathbf{x}}\hat{\mathbf{y}}(\beta)} = \hat{\mathbf{y}}(\beta) - \hat{\mathbf{x}} = [R\cos\beta - r\cos\gamma, R\sin\beta - r\sin\gamma]^T.$$

Let L be the magnitude of this vector. It follows that

$$\begin{aligned} L &= \|\overrightarrow{\hat{\mathbf{x}}\hat{\mathbf{y}}(\beta)}\| \\ &= \|\hat{\mathbf{x}} - \hat{\mathbf{y}}(\beta)\| \\ &= \sqrt{< \hat{\mathbf{x}} - \hat{\mathbf{y}}(\beta), \hat{\mathbf{x}} - \hat{\mathbf{y}}(\beta) >} \\ &= \sqrt{\|\hat{\mathbf{x}}\|^2 + \|\hat{\mathbf{y}}(\beta)\|^2 - 2 < \hat{\mathbf{x}}, \hat{\mathbf{y}}(\beta) >} \\ &= \sqrt{r^2 + R^2 - 2rR\cos(\gamma - \beta)}. \end{aligned}$$

Let ψ be the polar angle of the vector from $\hat{\mathbf{x}}$ to $\hat{\mathbf{y}}(\beta)$. Then

$$\cos\psi = \frac{R\cos\beta - r\cos\gamma}{L} \quad \text{and} \quad \sin\psi = \frac{R\sin\beta - r\sin\gamma}{L}.$$

We may relate this geometry to the fan-beam geometry for 2-D CT. See [5] or [13] for more on the fan-beam geometry. Let $\phi = \psi + \pi/2$. We define α to be the angle between the line from $\hat{\mathbf{y}}(\beta)$ to $\hat{\mathbf{x}}$ and the line from $\hat{\mathbf{y}}(\beta)$ to the origin. We take α to be positive if the line from $\hat{\mathbf{y}}(\beta)$ to $\hat{\mathbf{x}}$ lies to the right of the line from $\hat{\mathbf{y}}(\beta)$ to the origin, when viewed from $\hat{\mathbf{y}}(\beta)$. Because $\psi = \beta - \alpha$, it follows that $\alpha = \beta - \psi = \beta - \phi + \pi/2$. Using the above relations for $\cos\psi$ and $\sin\psi$, we find that

$$\begin{aligned}
\sin\alpha &= \sin(\beta - \psi) \\
&= \sin\beta\cos\psi - \cos\beta\sin\psi \\
&= \frac{\sin\beta(R\cos\beta - r\cos\gamma) - \cos\beta(R\sin\beta - r\sin\gamma)}{L} \\
&= \frac{r(\sin\gamma\cos\beta - \cos\gamma\sin\beta)}{L} \\
&= \frac{r\sin(\gamma - \beta)}{L}
\end{aligned}$$

and

$$\begin{aligned}
\cos\alpha &= \cos(\beta - \psi) \\
&= \cos\beta\cos\psi + \sin\beta\sin\psi \\
&= \frac{\cos\beta(R\cos\beta - r\cos\gamma) + \sin\beta(R\sin\beta - r\sin\gamma)}{L} \\
&= \frac{R - r(\cos\gamma\cos\beta + \sin\gamma\sin\beta)}{L} \\
&= \frac{R - r\cos(\gamma - \beta)}{L}.
\end{aligned}$$

Hence,

$$\tan\alpha = \frac{\sin\alpha}{\cos\alpha} = \frac{r\sin(\gamma - \beta)}{R - r\cos(\gamma - \beta)}.$$

Because $\alpha \in (-\pi/2, \pi/2)$, we may write

$$\alpha = \arcsin\left(\frac{r\sin(\gamma - \beta)}{L}\right) \tag{3.5}$$

and

$$\alpha = \arctan\left(\frac{r\sin(\gamma-\beta)}{R - r\cos(\gamma-\beta)}\right). \tag{3.6}$$

Define the fan-beam transform

$$Dg(\mathbf{z},\boldsymbol{\omega}) = \int_0^\infty g(\mathbf{z}+\mathrm{t}\boldsymbol{\omega})\mathrm{dt}, \qquad \mathbf{z}\in\mathbb{R}^2, \boldsymbol{\omega}\in \mathrm{S}^1 = \text{ unit circle.}$$

The fan-beam transform may be re-parameterized as $Dg(\beta,\alpha) = Dg(\mathbf{z},\boldsymbol{\omega})$, where β and α are as defined above. Faridani [5] shows that the fan-beam transform enjoys the symmetry relation $Df(\beta,\alpha) = Df(\beta+\pi-2\alpha,-\alpha)$ (note that he uses a definition for α which is the negative of ours). From this symmetry relation, we see that

$$\beta' = \beta + \pi - 2\alpha. \tag{3.7}$$

Using equations 3.5 and 3.7 together, β' can be expressed in terms of γ and β. Hence, given $\hat{\mathbf{x}}$ and $\hat{\mathbf{y}}(\beta)$, we can find $\hat{\mathbf{y}}(\beta')$.

Now, let $\hat{\mathbf{y}}(s_b)$ and $\hat{\mathbf{y}}(s_t)$ denote the orthogonal projections of $\mathbf{y}(s_b)$ and $\mathbf{y}(s_t)$ onto the x_1-x_2 plane. When the PI-line segment is projected onto the x_1-x_2 plane, the endpoints $\mathbf{y}(s_b)$ and $\mathbf{y}(s_t)$ of the projected segment must be related by equation 3.7, where $\beta = s_b$ and $\beta' = s_t$. Therefore, $s_t = s_b+\pi-2\alpha$.

Next, note that

$$L := \|\hat{\mathbf{y}}(s_b) - \hat{\mathbf{x}}\| = \sqrt{R^2 + r^2 - 2rR\cos(\gamma - s_b)}$$

and

$$\begin{aligned}
d &:= \|\hat{\mathbf{y}}(s_t) - \hat{\mathbf{y}}(s_b)\| \\
&= R\sqrt{(\cos s_t - \cos s_b)^2 + (\sin s_t - \sin s_b)^2} \\
&= R\sqrt{\cos^2 s_t - 2\cos s_t\cos s_b + \cos^2 s_b + \sin^2 s_t - 2\sin s_t \sin s_b + \sin^2 s_b} \\
&= R\sqrt{2 - 2(\cos s_t\cos s_b + \sin s_t \sin s_b)} \\
&= R\sqrt{2 - 2\cos(s_t - s_b)} \\
&= R\sqrt{2(1-\cos(\pi - 2\alpha))} \\
&= R\sqrt{2(1+\cos(2\alpha))} \\
&= R\sqrt{4\cos^2\alpha} \\
&= 2R|\cos(\alpha)| \\
&= 2R\cos(\alpha) \qquad \text{since } \alpha\in(-\pi/2,\pi/2).
\end{aligned}$$

Consider the plane parallel to the x_3-axis and containing the PI-line. We choose the coordinate vectors $(1/d)(\hat{\mathbf{y}}(s_t)-\hat{\mathbf{y}}(s_b))$ and $\mathbf{e}_3$ for this plane. The slope of the PI-line in this plane with respect to the chosen coordinate vectors is $m = h(s_t-s_b)/d$ (recall that $h = P/(2\pi)$). Hence, in this plane, the PI-line satisfies the equation

$$x_3 = \frac{h(s_t - s_b)}{d} L + h s_b.$$

Now, we may use $s_t = s_b + \pi - 2\alpha$, the relation for $\cos\alpha$, and equation 3.5 to write

$$\begin{aligned} x_3 &= \frac{h(\pi - 2\alpha)}{d} L + h s_b \\ &= \frac{h(\pi - 2\arcsin(\frac{r\sin(\gamma - s_b)}{L}))L^2}{2R(R - r\cos(\gamma - s_b))} + h s_b. \end{aligned}$$

Alternatively, using equation 3.6 and the relation for L yields

$$\begin{aligned} x_3 &= \frac{h(\pi - 2\alpha)}{d} L + h s_b \\ &= \frac{h(\pi - 2\arctan(\frac{r\sin(\gamma - s_b)}{R - r\cos(\gamma - s_b)}))L^2}{2R(R - r\cos(\gamma - s_b))} + h s_b \\ &= h\left(\pi - 2\arctan\left(\frac{r\sin(\gamma - s_b)}{R - r\cos(\gamma - s_b)}\right)\right) \times \frac{R^2 + r^2 - 2rR\cos(\gamma - s_b)}{2R(R - r\cos(\gamma - s_b))} + h s_b \\ &= h\left(\pi - 2\arctan\left(\frac{r\sin(\gamma - s_b)}{R - r\cos(\gamma - s_b)}\right)\right) \times \frac{R^2 + r^2 - 2rR\cos(\gamma - s_b) + R^2 - R^2}{2R(R - r\cos(\gamma - s_b))} + h s_b \\ &= h\left(\pi - 2\arctan\left(\frac{r\sin(\gamma - s_b)}{R - r\cos(\gamma - s_b)}\right)\right) \times \frac{2R(R - r\cos(\gamma - s_b)) + r^2 - R^2}{2R(R - r\cos(\gamma - s_b))} + h s_b \\ &= h\left[\left(\pi - 2\arctan\left(\frac{r\sin(\gamma - s_b)}{R - r\cos(\gamma - s_b)}\right)\right) \times \left(1 + \frac{r^2 - R^2}{2R(R - r\cos(\gamma - s_b))}\right) + s_b\right]. \end{aligned}$$

By the definition of a PI-line, $s_t \leq s_b + 2\pi$. Inserting this relation into $hs_b \leq x_3 \leq hs_t$ yields $hs_b \leq x_3 \leq hs_b + 2\pi h$. Performing some simple algebra, we then find that s_b must satisfy

$$\frac{x_3}{h} - 2\pi \leq s_b \leq \frac{x_3}{h}.$$

□

3.4 Algorithm Summary

Theorem 3 suggests an algorithm for the flat detector, which is outlined below. Additional implementation details will be discussed in the next section.

1) Calculate derivative via chain rule:

$$g_1(s,u,w) = \frac{\partial}{\partial q} Df(\mathbf{y}(\mathrm{q}), \boldsymbol{\theta}_f(s,x,\gamma)\Big|_{q=s} = (\frac{\partial g_f}{\partial q} + \frac{u^2+D^2}{D}\frac{\partial g_f}{\partial u} + \frac{uw}{D}\frac{\partial g_f}{\partial w})\Big|_{q=s}$$

Alternatively, the derivative may be implemented directly without using the chain rule (see next section).

2) Length correction weighting:

$$g_2(s,u,w) = \frac{D}{\sqrt{u^2+D^2+w^2}} g_1(s,u,w)$$

3) Forward height rebinning:
Let r be the maximum object radius. Also, the half fan angle is given by $\alpha_m = \arcsin(r/R)$. Use linear interpolation to compute for all $\psi_n \in [-\pi/2 - \alpha_m, \pi/2 + \alpha_m]$

$$g_3(s,u,\psi) = g_2(s,u,w_k(u,\psi)),$$

where

$$w_\kappa(u,\psi) = \frac{Dh}{R}\left(\psi + \frac{\psi}{\tan(\psi)}\frac{u}{D}\right).$$

4) 1-D Hilbert transform in u
At constant ψ, compute

$$g_4(s,u,\psi) = \int_{-\infty}^{\infty} k_H(u-u') g_3(s,u',\psi) du'$$

5) Backward height rebinning
Compute

$$g_5(s,u,w) = g_4(s,u,\hat{\psi}(u,w)),$$

where $\hat{\psi}(u,w)$ is the angle ψ of smallest absolute value that satisfies

$$w = \frac{Dh}{R}\left(\psi + \frac{\psi}{\tan(\psi)}\frac{u}{D}\right).$$

So we see that $g_5(s,u_0,w_0)$ is obtained from a convolution of the data $g_2(s,u,w)$ on the κ-line of smallest $|\psi|$ value passing through (u_0,w_0).

6) Backprojection
First, use Kyle Champley's method for finding the PI-intervals. This requires solving a nonlinear equation for s_b for each x. Then compute the backprojection,

$$f(x) = \frac{1}{2\pi}\int_{s_b}^{s_t} \frac{g_5(s,u^*,w^*)}{v^*(s,x)}ds.$$

MATLAB code for this algorithm is provided in the appendix.

3.5 Additional Implementation Details

Assume the detector has M rows and N columns. Discretize the detector coordinates via

$$u_i = (i-1-N/2)\Delta u \quad i = 1,2,\ldots,N$$
$$w_j = (j-1-M/2)\Delta w \quad j = 1,2,\ldots,M$$

and assume that s is discretized as s_k for some range of k.

1) As suggested by Noo et al. [15], the derivative via the chain rule may be implemented with differences as follows:

$$\begin{aligned} g_1(s_{k+1/2},u_{i+1/2},w_{j+1/2}) \approx & \sum_{m=i}^{i+1}\sum_{n=j}^{j+1}\frac{g_f(s_{k+1},u_m,w_n)-g_f(s_k,u_m,w_n)}{4\Delta s} \\ & + \left(\frac{u_{i+1/2}^2+D^2}{D}\right)\sum_{p=k}^{k+1}\sum_{n=j}^{j+1}\frac{g_f(s_p,u_{i+1},w_n)-g_f(s_p,u_i,w_n)}{4\Delta u} \\ & + \left(\frac{u_{i+1/2}w_{j+1/2}}{D}\right)\sum_{p=k}^{k+1}\sum_{m=i}^{i+1}\frac{g_f(s_p,u_m,w_{j+1})-g_f(s_p,u_m,w_j)}{4\Delta w}. \end{aligned}$$

Note that the above discretization of (s, u, w) was chosen so that after the derivative step, the grid is centered around the detector origin.

Alternatively, Noo et al. suggest that the derivative may be taken directly without using the chain rule. This approach may be implemented with the difference

$$\begin{aligned} g_1(s_{k+1/2}, u, w) &\approx \frac{g(s_{k+1}, \boldsymbol{\theta}_f(s_{k+1/2}, u, w) - g(s_k, \boldsymbol{\theta}_f(s_{k+1/2}, u, w))}{\Delta s} \\ &\approx \frac{g_f(s_{k+1}, u_{\text{right}}, w_{\text{right}}) - g_f(s_k, u_{\text{left}}, w_{\text{left}})}{\Delta s}, \end{aligned}$$

where u_{right}, w_{right}, u_{left}, and w_{left} are determined using equations (3.1),(3.2), and (3.3). Noo et al. found that the chain rule approach to the derivative produced superior results compared to the direct approach. Therefore, the chain rule approach was used for the reconstructions in this paper.

4) To implement this step, we must both regularize and sample the Hilbert transform in an appropriate sense. Recall that the Hilbert transform kernel may be formally expressed as

$$k_H(t) = -\int_{-\infty}^{\infty} i \ \text{sgn}(\xi) e^{i2\pi\xi t} d\xi.$$

Let b denote a cut-off frequency for the kernel. Then we may write

$$\begin{aligned} k_H(t) &\approx -\int_{-b}^{b} i \ \text{sgn}(\xi) e^{i2\pi\xi t} d\xi \\ &= \int_{-b}^{0} i \ e^{i2\pi\xi t} d\xi - \int_{0}^{b} i \ e^{i2\pi\xi t} d\xi \\ &= \left[\frac{1}{2\pi t} e^{i2\pi\xi t}\right]_{\xi=-b}^{0} - \left[\frac{1}{2\pi t} e^{i2\pi\xi t}\right]_{\xi=0}^{b} \\ &= \frac{1}{2\pi t}\left[1 - e^{-i2\pi bt} - e^{i2\pi bt} + 1\right] \\ &= \frac{1}{2\pi t}\left[2 - 2\cos(2\pi bt)\right] \\ &= \frac{1}{\pi t}\left[1 - \cos(2\pi bt)\right]. \end{aligned}$$

Now sample t by letting $t_n = n\Delta t$. In order to avoid aliasing errors, the cut-off frequency must satisfy the Nyquist condition $b \leq b_{\max} = 1/(2\Delta t)$. Letting $b = b_{\max}$ yields the discrete kernel

$$\begin{aligned} k_H[n] &= \frac{1}{\pi n \Delta t}\left[1 - \cos(\pi n)\right] \\ &= \begin{cases} \frac{2}{\pi n \Delta t} & \text{if } n \text{ is odd} \\ 0 & \text{if } n \text{ is even.} \end{cases} \end{aligned}$$

In addition, it is necessary to window the Hilbert kernel in the frequency domain to reduce ringing artifacts. For example, let $\mathrm{win}[n]$ be the inverse Fourier transform of a Hamming window. Then we can use the modified kernel $k_W[n] = \mathrm{win}[n] * k_H[n]$, where "$*$" denotes convolution.

Let $u_n = n\Delta u$. The trapezoidal rule may be used to write the modified discrete Hilbert transform

$$g_4(s, u_n, \psi) = \Delta u \sum_{k=k_{\min}}^{k_{\max}} k_W[n-k] g_3(s, u_k, \psi).$$

This is a discrete convolution and may be implemented using FFTs.

5) We want to find $g_5(s, u, w) = g_4(s, u, \hat{\psi}(u, w))$ where $\hat{\psi}(u, w)$ is the angle ψ of smallest absolute value that satisfies the κ-line equation

$$w = \frac{Dh}{R}\left(\psi + \frac{\psi}{\tan(\psi)}\frac{u}{D}\right).$$

In order to avoid direct solution of the above equation, Noo et al. suggest a nice trick. We may take g_5 to be a linear interpolation of g_4. Specifically,

$$g_5(s, u_i, w) \approx (1 - c(u_i, w, l)) g_4(s, u_i, \psi_l) + c(u_i, w, l) g_4(s, u_i, \psi_{l+1}),$$

where $w_\kappa(u_i, \psi_l) \leq w_j \leq w_\kappa(u_i, \psi_{l+1})$ and $c(u_i, w, l) = (w - w_\kappa(u_i, \psi_l))/(w_\kappa(u_i, \psi_{l+1}) - w_\kappa(u_i, \psi_l))$. For $u_i \geq 0$, loop over j and l as long as $w_\kappa(u_i, \psi_{l+1}) > w_\kappa(u_i, \psi_l)$ until $w_\kappa(u_i, \psi_l) \leq w_j \leq w_\kappa(u_i, \psi_{l+1})$, with l going from $l = -M$ to $l = M$. Then for $u_i < 0$, loop over j and l as long as $w_\kappa(u_i, \psi_{l-1}) < w_\kappa(u_i, \psi_l)$ until $w_\kappa(u_i, \psi_{l-1}) \leq w_j \leq w_\kappa(u_i, \psi_l)$, with l going from $l = M$ to $l = -M$.

Referring to Figure 3.2, we see that κ-lines may cross outside of the Tam-Danielsson window near the upper right and lower left corners. The change

of loop direction above depending on the sign of u_i is sufficient to guarantee that g_5 is estimated using the κ-line with smallest $|\psi|$.

6) Any root finding algorithm may be used to solve the non-linear equation for s_b (and hence s_t)). In order to avoid artifacts, it is important to require that the tolerance on the root finder depends on the helical pitch. In particular, the tolerance should become smaller for smaller helical pitches.

Also, to avoid artifacts it is important to treat the endpoints of the back-projection integration in a smooth manner. Noo et al. [15] suggest computing the back-projection via

$$f(\mathbf{x}) \approx \sum_k \frac{\rho(s_k, \mathbf{x})\Delta \mathrm{s}}{2\pi v^*(s_k, \mathbf{x})} g_f^F(s_k, u^*(s_k, \mathbf{x}), w^*(s_k, \mathbf{x})),$$

where

$$\rho(s, \mathbf{x}) = \begin{cases} 0 & \text{if } s \leq s_b - \Delta s \\ (1 + d_b)^2/2 & \text{if } s_b - \Delta s \leq s \leq s_b \\ \frac{1}{2} + d_b - d_b^2/2 & \text{if } s_b \leq s \leq s_b + \Delta s \\ 1 & \text{if } s_b + \Delta s \leq s \leq s_t - \Delta s \\ \frac{1}{2} + d_t - d_t^2/2 & \text{if } s_t - \Delta s \leq s \leq s_t \\ (1 + d_t)^2/2 & \text{if } s_t \leq s \leq s_t + \Delta s \\ 0 & \text{if } s \geq s_t + \Delta s \end{cases}$$

and

$$d_b = \frac{s - s_b(\mathbf{x})}{\Delta s} \qquad d_t = \frac{s_t(\mathbf{x}) - \mathrm{s}}{\Delta s}.$$

In order to evaluate g_f^F at (s_k, u^*, w^*), interpolation is necessary. Nearest neighbor interpolation was used for all reconstructions in this paper. In addition, an optional pre-interpolation step is included in the MATLAB code provided in the Appendix. Pre-interpolation was not used for any of the reconstructions in Chapter 5 because it was found to have little impact.

3.6 Computational Complexity

Now, we will examine the computational requirements of this algorithm. Let M be the number of detector rows, let N be the number of detector columns, let K be the number of source positions per turn, let L be the number of

filtering lines on the detector plane, and let the reconstruction size of a slice be $M_x \times M_y$. Then the dominant steps in the reconstruction for a single slice have the complexities listed in Table 3.1. If we assume that K, L, N, M_x, and M_y are all proportional to M, then the complexities of the steps in the algorithm take the simplified form in Table 3.2. If the detector height is held constant, then $M = O(\Delta w^{-1})$.

Looking at Table 3.2, we see that the backward height rebinning has the largest asymptotic bound. However, in practice the filtering and backprojection steps dominate the computation. For small N, the back-projection step uses the most time, but for large N, the filtering step will require more time than the back-projection.

derivative	$O(KMN)$
forward height rebinning	$O(KNL)$
filtering	$O(KLN \log_2(N))$
backward height rebinning	$O(KMNL)$
back-projection	$O(M_x M_y K)$

Table 3.1: Computational complexities for the Katsevich algorithm applied to a single slice

derivative	$O(M^3)$
forward height rebinning	$O(M^3)$
filtering	$O(M^3 \log_2(M))$
backward height rebinning	$O(M^4)$
back-projection	$O(M^3)$

Table 3.2: Simplified computational complexities for the Katsevich algorithm applied to a single slice

Chapter 4

Implementation for a Curved Detector

The implementation of Katsevich's formula for a curved detector is very similar to the flat detector case, but with some important modifications. We will follow the implementation details of Noo et al. [15].

4.1 Curved Detector Geometry

Let α be the polar angle of rays relative to the line through $\mathbf{y}(s)$ and the center of the detector. Then for a curved detector, we introduce the local detector coordinates (α, v, w) (see Figure 4.1). The curved detector coordinates (α, v_c, w_c) may be converted to the flat detector coordinates (u, v_f, w_f) via

$$u = D\tan\alpha \quad v_f = v_c \quad w_f = \frac{w_c}{\cos\alpha}. \tag{4.1}$$

Given (α, u, w), we may express the x-ray projection data with these local coordinates as

$$g_c(s, \alpha, w) = Df(\mathbf{y}(\mathrm{s}), \boldsymbol{\theta}_c)$$

where the subscript "c" means that the data is for a curved detector. In the above formula,

$$\boldsymbol{\theta}_c(s, \alpha, w) = \frac{1}{\sqrt{D^2 + w^2}}(D\sin\alpha\ \mathbf{e}_u(s) + D\cos\alpha\ \mathbf{e}_v(s) + w\mathbf{e}_w) \tag{4.2}$$

is a unit vector in the direction of the ray which passes through $\mathbf{y}(\mathrm{s})$ and which intersects the detector at coordinates (α, w).

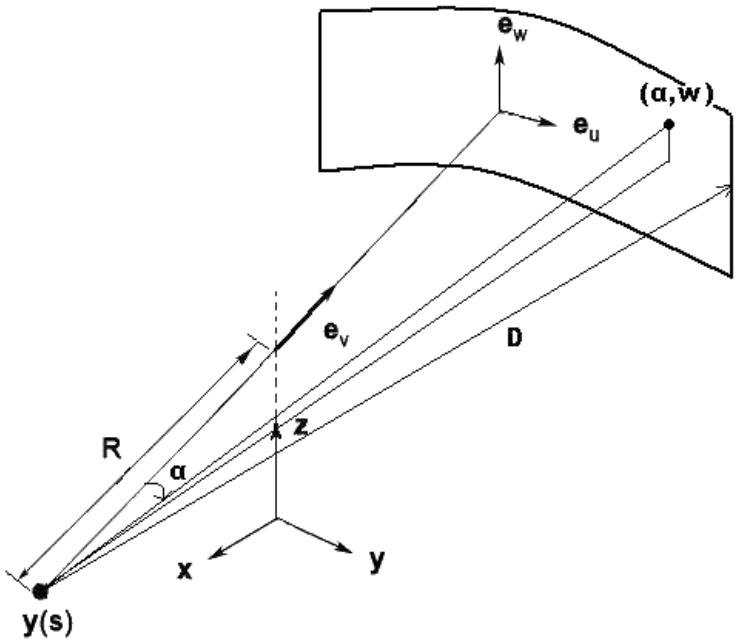

Figure 4.1: Curved Detector Geometry

Also, given $(s, \boldsymbol{\theta})$, we can express the projection data in terms of detector coordinates. Using equations (3.2) and (4.1), we see that

$$\alpha_c = \arctan\left(\frac{< \boldsymbol{\theta}, \mathbf{e}_{\mathrm{u}}(\mathrm{s}) >}{< \boldsymbol{\theta}, \mathbf{e}_{\mathrm{v}}(\mathrm{s}) >}\right). \tag{4.3}$$

Let γ be the angle between $\boldsymbol{\theta}$ and $\mathbf{e}_{\mathrm{w}}$. Then

$$w_c = D\cot\gamma = D\frac{< \boldsymbol{\theta}, \mathbf{e}_{\mathrm{w}} >}{\sqrt{1 - < \boldsymbol{\theta}, \mathbf{e}_{\mathrm{w}} >^2}}. \tag{4.4}$$

Hence, (α_c, w_c) are the local coordinates of the intersection of the line with direction $\boldsymbol{\theta}$ and source point $\mathbf{y}(\mathrm{s})$ with the detector, and we may write

$$Df(\mathbf{y}(\mathrm{s}), \boldsymbol{\theta}) = g_c(s, \alpha_c, w_c).$$

Write the unit vector pointing from $\mathbf{y}(\mathrm{s})$ toward $\mathbf{x}$ as

$$\boldsymbol{\beta}(s, \mathbf{x}) = \frac{\mathbf{x} - \mathbf{y}(\mathrm{s})}{\|\mathbf{x} - \mathbf{y}(\mathrm{s})\|}.$$

Then it follows from the formulas of §3.1 and equations (4.1) that

$$Df(\mathbf{y}(\mathrm{s}), \boldsymbol{\beta}) = g_c(s, \alpha^*, w^*),$$

where

$$v^*(s, \mathbf{x}) = R - x_1 \cos(s) - x_2 \sin(s),$$

$$\alpha^*(s, \mathbf{x}) = \arctan\left(\frac{1}{v^*(s, x)}(-x_1 \sin(s) + x_2 \cos(s))\right),$$

and

$$w^*(s, \mathbf{x}) = \frac{D \cos \alpha^*(s, \mathbf{x})}{v^*(s, x)}(x_3 - hs).$$

Here (α^*, w^*) are the coordinates for the point of intersection of the detector with the line passing through $y(s)$ and $\mathbf{x}$.

4.2 The Katsevich Formula in Local Curved Detector Coordinates

In this section, we will express the Katsevich formula in the local curved detector coordinates.

Lemma 6 *The equation for the κ-curve of angle ψ is*

$$w_\kappa = \frac{DP}{2\pi R}\left(\psi \cos \alpha + \frac{\psi \sin \alpha}{\tan \psi}\right).$$

Proof:
From Lemma 1 for the flat detector, we have

$$w_\kappa = \frac{DP}{2\pi R}\left(\psi + \frac{\psi}{D \tan \psi} u\right).$$

Using equations (4.1), yields the κ-curve for the curved detector.

$$\begin{aligned} w_\kappa &= \frac{DP}{2\pi R}\cos\alpha\left(\psi + \frac{\psi\tan\alpha}{\tan\psi}u\right) \\ &= \frac{DP}{2\pi R}\left(\psi\cos\alpha + \frac{\psi\sin\alpha}{\tan\psi}u\right) \end{aligned}$$

□

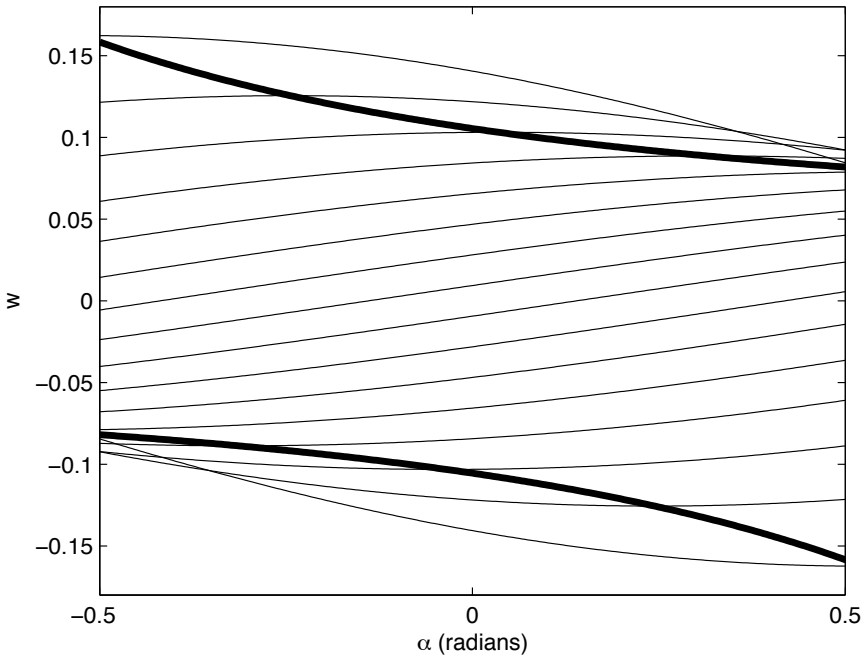

Figure 4.2: κ-curves on a Curved Detector, The dark curves are the edges of the Tam-Danielsson window.

Recall from chapter 2, that Katsevich's formula may be rewritten using the definitions

$$g'(s,\boldsymbol{\eta}(s,\mathbf{x})) = \frac{\partial}{\partial q}Df(\mathbf{y}(q),\boldsymbol{\eta}(s,\mathbf{x}))\Big|_{q=s}$$

and

$$g^F(s,\boldsymbol{\eta}(s,\mathbf{x})) = PV\int_0^{2\pi} k_H(\sin\gamma)g'(s,\cos(\delta-\gamma)\boldsymbol{\beta}(s,\mathbf{x})-\sin(\delta-\gamma)\mathbf{e}(s,\mathbf{x}))\,d\gamma,$$

where $\boldsymbol{\eta}(s,\mathbf{x}) = \cos\delta\boldsymbol{\beta}(\mathrm{s},\mathbf{x}) + \sin\delta\mathbf{e}(s,\mathbf{x})$ for some $\delta \in [0,2\pi)$. Note that $\boldsymbol{\eta}$ is independent of q in the derivative formula. Then the Katsevich formula takes the form

$$f(\mathbf{x}) = -\frac{1}{2\pi}\int_{\mathrm{I_{PI}(x)}} \frac{1}{\|\mathbf{x}-\mathbf{y}(s)\|}\mathrm{g^F}(\mathrm{s},\boldsymbol{\beta}(\mathrm{s},\mathbf{x}))\,ds.$$

Next, we will write these formulas in terms of detector coordinates.

Recall that $g_f(s,\alpha,w) = Df(\mathbf{y}(\mathrm{s}),\boldsymbol{\theta}_\mathrm{c})$ where $\boldsymbol{\theta}_c(s,\alpha,w)$ is a unit vector in the direction of the line which passes through $\mathbf{y}(\mathrm{s})$ and intersects the detector at (α,w). We define

$$g_1(s,\alpha,w) := g'(s,\boldsymbol{\theta}_c(s,\alpha,w)) = \frac{\partial}{\partial q}Df(\mathbf{y}(q),\boldsymbol{\theta}_c(s,\alpha,w))\Big|_{q=s}$$

and have the following lemma.

Lemma 7

$$g_1(s,\alpha,w) = (\frac{\partial g_c}{\partial q} + \frac{\partial g_c}{\partial \alpha})\Big|_{q=s}$$

Proof:
Using the chain rule, we have

$$g_1(s,\alpha,w) = \frac{\partial}{\partial q}Df(\mathbf{y}(\mathrm{q}),\boldsymbol{\theta}_c(s,\alpha,w)\Big|_{q=s} = (\frac{\partial g_c}{\partial q} + \frac{\partial g_c}{\partial \alpha}\frac{\partial \alpha_c}{\partial q} + \frac{\partial g_c}{\partial w}\frac{\partial w_c}{\partial q})\Big|_{q=s}.$$

Using equations (4.3) and (4.4),

$$\alpha_c = \arctan\left(\frac{<\boldsymbol{\theta}_c,\mathbf{e}_\mathrm{u}(\mathrm{q})>}{<\boldsymbol{\theta}_c,\mathbf{e}_\mathrm{v}(\mathrm{q})>}\right) \quad \text{and} \quad w_c = D\frac{<\boldsymbol{\theta}_c,\mathbf{e}_\mathrm{w}>}{\sqrt{1-<\boldsymbol{\theta}_c,\mathbf{e}_\mathrm{w}>^2}}.$$

Since w_c is independent of $q, \frac{\partial w_c}{\partial q} = 0$. In addition,

$$\begin{aligned}
\frac{\partial \alpha_c}{\partial q} &= \frac{1}{1+\left(\frac{<\boldsymbol{\theta}_c,\mathbf{e}_\mathrm{u}>}{<\boldsymbol{\theta}_c,\mathbf{e}_\mathrm{v}>}\right)^2}\frac{\partial}{\partial q}\left(\frac{<\boldsymbol{\theta}_c,\mathbf{e}_\mathrm{u}(\mathrm{q})>}{<\boldsymbol{\theta}_c,\mathbf{e}_\mathrm{v}(\mathrm{q})>}\right) \\
&= \frac{1}{1+\left(\frac{<\boldsymbol{\theta}_c,\mathbf{e}_\mathrm{u}>}{<\boldsymbol{\theta}_c,\mathbf{e}_\mathrm{v}>}\right)^2}\left(\frac{<\boldsymbol{\theta}_c,\mathbf{e}_\mathrm{v}>^2+<\boldsymbol{\theta}_\mathrm{c},\mathbf{e}_\mathrm{u}>^2}{<\boldsymbol{\theta}_c,\mathbf{e}_\mathrm{v}>^2}\right) \\
&= \left(\frac{1}{1+\tan^2\alpha_c}\right)\frac{D^2\cos^2\alpha_c + D^2\sin^2\alpha_c}{D^2\cos^2\alpha_c} \\
&= \left(\frac{1}{1+\tan^2\alpha_c}\right)\frac{1}{\cos^2\alpha_c} \\
&= \frac{1}{\cos^2\alpha+\sin^2\alpha} \\
&= 1
\end{aligned}$$

Thus, we see that

$$g_1(s,\alpha,w) = (\frac{\partial g_c}{\partial q}+\frac{\partial g_c}{\partial \alpha})\Big|_{q=s}.$$

□

Lemma 8

$$g^F(s,\boldsymbol{\beta}) = -\frac{\sqrt{D^2+w_\kappa^2}}{D}\int_{-\pi/2}^{\pi/2} k_H(\sin(\alpha-\alpha'))\frac{D}{\sqrt{D^2+(w'_\kappa)^2}}g_1(s,\alpha',w'_\kappa)d\alpha',$$

where $(\alpha, w_\kappa(\alpha))$ *lies on a* κ*-curve for the curved detector.*

Proof:

Recall that Lemma 3 for the flat detector gave the formula

$$g^F(s,\boldsymbol{\beta}) = -\frac{r}{D}\int_{-\infty}^{\infty} k_H(u-u')\frac{D}{r'}g_1(s,u',w'_{f\kappa})du',$$

where $r = \sqrt{u^2+D^2+w_{f\kappa}^2}$ and $r' = \sqrt{(u')^2+D^2+(w'_{f\kappa})^2}$ are the distances from $\mathbf{y}(s)$ to the flat detector points $(u, w_{f\kappa}(u))$ and $(u', w'_{f\kappa}(u'))$, respectively. Here $w_{f\kappa}$ lies on a κ-line on the flat detector.

Using equations (4.1), it follows that

$$\begin{aligned} u - u' &= D(\tan\alpha - \tan\alpha') \\ &= D\left(\frac{\sin\alpha\cos\alpha' - \sin\alpha'\cos\alpha}{\cos\alpha\cos\alpha'}\right) \\ &= D\left(\frac{\sin(\alpha-\alpha')}{\cos\alpha\cos\alpha'}\right). \end{aligned}$$

Also,

$$\begin{aligned} du' &= \frac{du'}{d\alpha'}d\alpha' \\ &= \frac{d}{d\alpha'}(D\tan\alpha')d\alpha' \\ &= D\sec^2\alpha' d\alpha' \\ &= \frac{D}{\cos^2\alpha'}d\alpha'. \end{aligned}$$

Hence,

$$\begin{aligned} k_H(u-u')du' &= k_H(\sin(\alpha-\alpha'))\frac{\cos\alpha\cos\alpha'}{D}\frac{D}{\cos^2\alpha'}d\alpha' \\ &= k_H(\sin(\alpha-\alpha'))\frac{\cos\alpha}{\cos\alpha'}d\alpha'. \end{aligned}$$

In addition,

$$\begin{aligned} r &= \sqrt{u^2 + D^2 + w_f^2} \\ &= \sqrt{D^2\tan^2\alpha + D^2 + \frac{w_c^2}{\cos^2\alpha}} \\ &= \frac{\sqrt{D^2\sin^2\alpha + D^2\cos^2\alpha + w_c^2}}{\cos\alpha} \\ &= \frac{\sqrt{D^2 + w_c^2}}{\cos\alpha}. \end{aligned}$$

Similarly,

$$r' = \frac{\sqrt{D^2 + (w_c')^2}}{\cos\alpha'}.$$

Using the above results, it follows that for the curved detector

$$g^F(s,\boldsymbol{\beta}) = -\frac{\sqrt{D^2+w_\kappa^2}}{D}\int_{-\pi/2}^{\pi/2} k_H(\sin(\alpha-\alpha'))\frac{D}{\sqrt{D^2+(w'_\kappa)^2}}g_1(s,\alpha',w'_\kappa)d\alpha'.$$

□

Lemma 9 *Let*

$$g_c^F(s,\alpha,w_\kappa) := \cos\alpha\int_{-\pi/2}^{\pi/2} k_H(\sin(\alpha-\alpha'))\frac{D}{\sqrt{D^2+(w'_\kappa)^2}}g_1(s,\alpha',w'_\kappa)d\alpha'.$$

Then

$$\frac{-1}{\|\mathbf{x}-\mathbf{y}(s)\|}g^F(s,\boldsymbol{\beta}) = \frac{1}{v^*(s,\mathbf{x})}g_c^F(s,\alpha,w_\kappa)$$

Proof:

Let $r=\sqrt{u^2+D^2+w_{f\kappa}^2}$ be the distance from $\mathbf{y}(s)$ to the flat detector point $(u,w_{f\kappa}(u))$, where $w_{f\kappa}$ lies on a κ-line on the flat detector. From the proof of Lemma 8, we have $r\cos\alpha = \sqrt{D^2+w_\kappa^2}$. Therefore, the result of Lemma 8 may be rewritten as

$$g^F(s,\boldsymbol{\beta}) = -\frac{r}{D}g_c^F(s,\alpha,w_\kappa).$$

By similar triangles,

$$\frac{r}{D} = \frac{\|\mathbf{x}-\mathbf{y}(s)\|}{<(\mathbf{x}-\mathbf{y}(s)),\mathbf{e}_v>} \qquad \Rightarrow \qquad \frac{r}{D\|\mathbf{x}-\mathbf{y}(s)\|} = \frac{1}{<(\mathbf{x}-\mathbf{y}(s)),\mathbf{e}_v>}.$$

As a consequence, we have

$$\begin{aligned}\frac{-1}{\|\mathbf{x}-\mathbf{y}(s)\|}g^F(s,\boldsymbol{\beta}) &= \frac{1}{\|\mathbf{x}-\mathbf{y}(s)\|}\frac{r}{D}g_c^F(s,\alpha,w_\kappa)\\ &= \frac{1}{<(\mathbf{x}-\mathbf{y}(s)),\mathbf{e}_v>}g_c^F(s,\alpha,w_\kappa)\\ &= \frac{1}{(R+<\mathbf{x},\mathbf{e}_{\mathrm{v}}>)}g_c^F(s,\alpha,w_\kappa)\\ &= \frac{1}{v^*(s,\mathbf{x})}g_c^F(s,\alpha,w_\kappa).\square\end{aligned}$$

Recall that the line passing through $\mathbf{y}(\mathrm{s})$ with direction $\boldsymbol{\beta}$ intersects the curved detector at (α^*, w^*). Collecting our results, we have proven the following theorem.

Theorem 4 (Katsevich formula in local curved detector coordinates) *Let $g_c(s,\alpha,w) := Df(\mathbf{y}(\mathrm{s}), \boldsymbol{\theta}_{\mathrm{c}})$, where*

$$\boldsymbol{\theta}_c(s,\alpha,w) = \frac{1}{\sqrt{D^2+w^2}}(D\sin\alpha\ \mathbf{e}_u(s) + D\cos\alpha\ \mathbf{e}_v(s) + w\mathbf{e}_{\mathrm{w}}).$$

Also, let v^*, α^*, and w^* be given by

$$v^*(s,\mathbf{x}) = R - x_1\cos(s) - x_2\sin(s),$$

$$\alpha^*(s,\mathbf{x}) = \arctan\left(\frac{1}{v^*}(-x_1\sin(s) + x_2\cos(s))\right),$$

and

$$w^*(s,\mathbf{x}) = \frac{D\cos\alpha^*}{v^*}(x_3 - hs).$$

Then the Katsevich formula may be written in local coordinates for a curved detector with the equations

$$g_1(s,\alpha,w) = \left(\frac{\partial g_c(q,\alpha,w)}{\partial q} + \frac{\partial g_c(q,\alpha,w)}{\partial \alpha}\right)\Big|_{q=s},$$

$$g_c^F(s,\alpha,w_\kappa) = \cos\alpha\int_{-\pi/2}^{\pi/2} k_H(\sin(\alpha-\alpha'))\frac{D}{\sqrt{D^2+(w'_\kappa)^2}}g_1(s,\alpha',w'_\kappa)d\alpha',$$

and

$$f(\mathbf{x}) = \frac{1}{2\pi}\int_{I_{PI}(\mathbf{x})}\frac{1}{v^*(s,\mathbf{x})}g_c^F(s,\alpha^*,w^*)\,ds.$$

4.3 Algorithm Summary

Theorem 4 suggests an algorithm for the curved detector, which is outlined below. Additional implementation details will be discussed in the next section.

1) Calculate derivative via chain rule:

$$g_1(s,\alpha,w) = \left(\frac{\partial g_c(q,\alpha,w)}{\partial q} + \frac{\partial g_c(q,\alpha,w)}{\partial \alpha} \right) \Big|_{q=s},$$

Alternatively, the derivative may be implemented directly without using the chain rule (see next section).

2) Length correction weighting:

$$g_2(s,\alpha,w) = \frac{D}{\sqrt{D^2+w^2}} g_1(s,\alpha,w)$$

3) Forward height rebinning:
Let r be the maximum object radius. Also, the half fan angle is given by $\alpha_m = \arcsin(r/R)$. Use linear interpolation to compute for all $\psi_n \in [-\pi/2 - \alpha_m, \pi/2 + \alpha_m]$

$$g_3(s,\alpha,\psi) = g_2(s,\alpha,w_k(\alpha,\psi)),$$

where

$$w_\kappa(\alpha,\psi) = \frac{Dh}{R} \left(\psi \cos\alpha + \frac{\psi}{\tan\psi} \sin\alpha \right).$$

4) 1-D Hilbert transform in u
At constant ψ, compute

$$g_4(s,\alpha,\psi) = \int_{-\pi/2}^{\pi/2} k_H(\sin(\alpha-\alpha')) g_3(s,\alpha',\psi) d\alpha'$$

5) Backward height rebinning
Compute

$$g_5(s, \alpha, w) = g_4(s, \alpha, \hat{\psi}(\alpha, w)),$$

where $\hat{\psi}(\alpha, w)$ is the angle ψ of smallest absolute value that satisfies

$$w = \frac{Dh}{R}\left(\psi \cos\alpha + \frac{\psi}{\tan\psi}\sin\alpha\right).$$

So we see that $g_5(s, \alpha_0, w_0)$ is obtained from a convolution of the data $g_2(s, \alpha, w)$ on the κ-line of smallest $|\psi|$ value passing through (α_0, w_0).

6) Post-Cosine Weighting
Compute

$$g_c^F(s, \alpha, w) = \cos\alpha g_5(s, \alpha, w).$$

7) Backprojection
First, use Kyle Champley's method for finding the PI-intervals, $[s_b(\mathbf{x}), s_t(\mathbf{x})]$. This requires solving a nonlinear equation for s_b for each $\mathbf{x}$. Then compute the backprojection,

$$f(x) = \frac{1}{2\pi}\int_{s_b}^{s_t} \frac{g_c^F(s, \alpha^*(s, \mathbf{x}), w^*(s, \mathbf{x}))}{v^*(s, \mathbf{x})} ds.$$

MATLAB code for this algorithm is provided in the appendix. Since the steps are very similar to the flat detector case, the computational complexity requirements are the same (see §3.6).

4.4 Additional Implementation Details

Assume the detector has M rows and N columns. Discretize the detector coordinates via

$$\alpha_i = (i - 1 - N/2)\Delta u \quad i = 1, 2, \ldots, N$$

$$w_j = (j - 1 - (M-1)/2)\Delta w \quad j = 1, 2, \ldots, M$$

and assume that s is discretized as s_k for some range of k.

Below, only details for the derivative step will be elaborated. The remaining details are very similar to the flat detector case.

1) As suggested by Noo et al. [15], the derivative via the chain rule may be implemented with differences as follows:

$$\begin{aligned} g_1(s_{k+1/2}, \alpha_{i+1/2}, w_j) \approx & \frac{g_c(s_{k+1}, \alpha_i, w_j) - g_c(s_k, \alpha_i, w_j)}{2\Delta s} \\ & + \frac{g_c(s_{k+1}, \alpha_{i+1}, w_j) - g_c(s_k, \alpha_{i+1}, w_j)}{2\Delta s} \\ & + \frac{g_c(s_k, \alpha_{i+1}, w_j) - g_c(s_k, \alpha_i, w_j)}{2\Delta \alpha} \\ & + \frac{g_c(s_{k+1}, \alpha_{i+1}, w_j) - g_c(s_{k+1}, \alpha_i, w_j)}{2\Delta \alpha}. \end{aligned}$$

Note that the above discretization of (s, α, w) was chosen so that after the derivative step, the grid is centered around the detector origin.

Noo et al. also show that the derivative may be taken directly without using the chain rule. This approach may be implemented with the difference

$$\begin{aligned} g_1(s_{k+1/2}, \alpha, w) &\approx \frac{g(s_{k+1}, \boldsymbol{\theta}_c(s_{k+1/2}, \alpha, w)) - g(s_k, \boldsymbol{\theta}_c(s_{k+1/2}, \alpha, w))}{\Delta s} \\ &\approx \frac{g_c(s_{k+1}, \alpha_{\text{right}}, w) - g_c(s_k, \alpha_{\text{left}}, w)}{\Delta s}, \end{aligned}$$

where

$$\alpha_{\text{right}} = \arctan\left(\frac{< \boldsymbol{\theta}_c(s_{k+1/2}, \alpha, w), \mathbf{e}_u(s_{k+1}) >}{< \boldsymbol{\theta}_c(s_{k+1/2}, \alpha, w), \mathbf{e}_v(s_{k+1}) >}\right)$$

and

$$\alpha_{\text{left}} = \arctan\left(\frac{< \boldsymbol{\theta}_c(s_{k+1/2}, \alpha, w), \mathbf{e}_u(s_k) >}{< \boldsymbol{\theta}_c(s_{k+1/2}, \alpha, w), \mathbf{e}_v(s_k) >}\right).$$

Using equation (4.2) and the definitions for $\mathbf{e}_{\text{u}}$ and $\mathbf{e}_{\text{v}}$, one may show that $\alpha_{\text{right}} = \alpha + \Delta s/2$ and $\alpha_{\text{left}} = \alpha - \Delta s/2$. Noo et al. found that the chain rule approach to the derivative produced superior results compared to the direct approach. Therefore, the chain rule approach was used for the reconstructions in this paper.

Chapter 5

Numerical Results

5.1 The FDK Algorithm

In 1984, Feldkamp, Davis, and Kress [7] proposed a filtered back-projection algorithm for cone-beam CT suitable for a circular scanning path. The FDK method uses an approximate inversion formula which is derived by adapting the fan-beam inversion formula to the cone-beam geometry. For details, see [14, §5.5.1]. In addition, the FDK algorithm may easily be extended to more general scanning paths, such as a helix, e.g. see Wang et al. [19].

Using the local detector coordinate notation of this paper, the FDK method for a flat detector with a helical scanning path takes the form

$$f_{FDK}(\mathbf{x}) = \frac{1}{2}\int_0^{2\pi} \frac{RD}{(v^*)^2}\int_{-\rho}^{\rho} k_b(u^*-u')g_f(s,u',w^*)\frac{Ddu'ds}{\sqrt{D^2+(u')^2+(w^*)^2}}.$$

where $g_f(s,u,w)$ is the cone-beam data in local coordinates,

$$v^*(s,\mathbf{x}) = R - x_1\cos(s) - x_2\sin(s),$$

$$u^*(s,\mathbf{x}) = \frac{D}{v^*(s,\mathbf{x})}(-x_1\sin(s)+x_2\cos(s)),$$

and

$$w^*(s,\mathbf{x}) = \frac{D}{v^*(s,\mathbf{x})}(x_3 - hs).$$

In addition, $k_b(u)$ is a filtering kernel (e.g. Shepp-Logan) appropriate for 2-D reconstruction. The implementation for the FDK method is straightforward and somewhat similar to the implementation for the filtering and

back-projection steps already provided for the Katsevich method. MATLAB code for this algorithm is provided in the appendix. We will use this method as a basis for comparison to the new Katsevich method.

Remark added July, 2010: My implementation of FDK for a helix had a mistake, so please disregard the FDK results. Also, I was told by Ryan Hass that the implementation of the backward rebinning step in my Katsevich code suffered from errors for very small helical pitch. So please disregard the convergence results for small pitch. For correct convergence results, please see:

Ryan Hass, PhD Thesis, Mathematics Dept., Oregon State Univ., 2009.

5.2 Phantoms

In order to perform reconstructions, we will use two synthetic test objects. For experiment 1, we will use the 3-D Shepp-Logan head phantom. For experiments 2 through 7, we will use a simpler phantom which is described below.

First, we define the functions

$$\begin{aligned} p_m(\mathbf{x}) &= (1 - \|\mathbf{x}\|)_+^m \\ &= \begin{cases} (1 - \|\mathbf{x}\|)^m & \text{if } 1 - \|\mathbf{x}\|^2 \geq 0 \\ 0 & \text{otherwise} \end{cases}. \end{aligned}$$

Note that if $m = 0$, then p_m becomes the indicator function for the unit ball centered at the origin. For $m > -1$ p_m is integrable. Also, if $m \geq 1$, then p_m is $m - 1$ times differentiable. It may be shown (e.g. see [6]) that the cone-beam transform of p_m is

$$Dp_m(\mathbf{y}, \boldsymbol{\theta}) = (1 - \|\mathbf{x}\|^2)_+^{\mathrm{m}+1/2} \left(2^{2\mathrm{m}+1} \frac{(\Gamma(\mathrm{m}+1))^2}{\Gamma(2\mathrm{m}+2)} \right).$$

Our phantoms consist of a superposition of copies p_m which are each rotated, dilated, and shifted. If $m = 0$, then these copies of p_m will become indicator functions of ellipsoids. Let A be a rotation and dilation matrix and

let $\mathbf{x}_0 \in \mathbb{R}^3$ be a fixed point. Given a function $f(\mathbf{x})$, we may define a rotated, dilated, and shifted version of it as

$$f_A(\mathbf{x}) = f(A(\mathbf{x} - \mathbf{x}_0)).$$

Then using properties of the cone-beam transform yields

$$Df_A(\mathbf{y}, \boldsymbol{\theta}) = \frac{1}{\|A\boldsymbol{\theta}\|} Df(A\mathbf{y}, \frac{A\boldsymbol{\theta}}{\|A\boldsymbol{\theta}\|}).$$

Since we know Dp_m, we may calculate the cone-beam transform for rotated, dilated, and shifted copies of p_m. Using the linearity of the cone-beam transform, we may then calculate the simulated cone-beam data for our phantom by summing up the contributions from each rotated, dilated, and shifted copy of p_m.

For the 3-D Shepp-Logan phantom, we let $m = 0$ and the rotated, dilated, and shifted copies of p_m become indicator functions for 10 ellipsoids with parameters similar to the 3-D Shepp-Logan head phantom of Kak and Slaney [9, p. 102]. Let a, b, and c be the half-axes of each ellipsoid. Let the center of each ellipsoid be given by $\mathbf{x}_0 = [\mathrm{x}_0, \mathrm{y}_0, \mathrm{z}_0]^{\mathrm{T}}$. Also, let β be the angle (in degrees) of rotation around the z-axis and let τ be the attenuation coefficient. The ten ellipsoids for our 3-D Shepp-Logan phantom have parameters given by Table 5.1.

ellipsoid	1	2	3	4	5	6	7	8	9	10
a	.69	.6624	.11	.16	.21	.046	.046	.046	.023	.023
b	.92	.874	.31	.41	.25	.046	.046	.023	.023	.046
c	.9	.88	.21	.22	.35	.046	.02	.02	.1	.1
x_0	0	0	.22	-.22	0	0	0	-.08	0	.06
y_0	0	-.0184	0	0	.35	.1	-.1	-.605	-.605	-.605
z_0	0	0	-.25	-.25	-.25	-.25	-.25	-.25	-.25	-.25
β	0	0	-18	18	0	0	0	0	0	0
τ	1	-.98	-.02	-.02	.01	.01	.01	.01	.01	.01

Table 5.1: Parameters for the 3-D Shepp-Logan head phantom

For the slice $z = -0.25$, the 3-D Shepp-Logan Phantom corresponds to the 2-D Shepp-Logan phantom. An image of the slice $z = -0.25$ from our

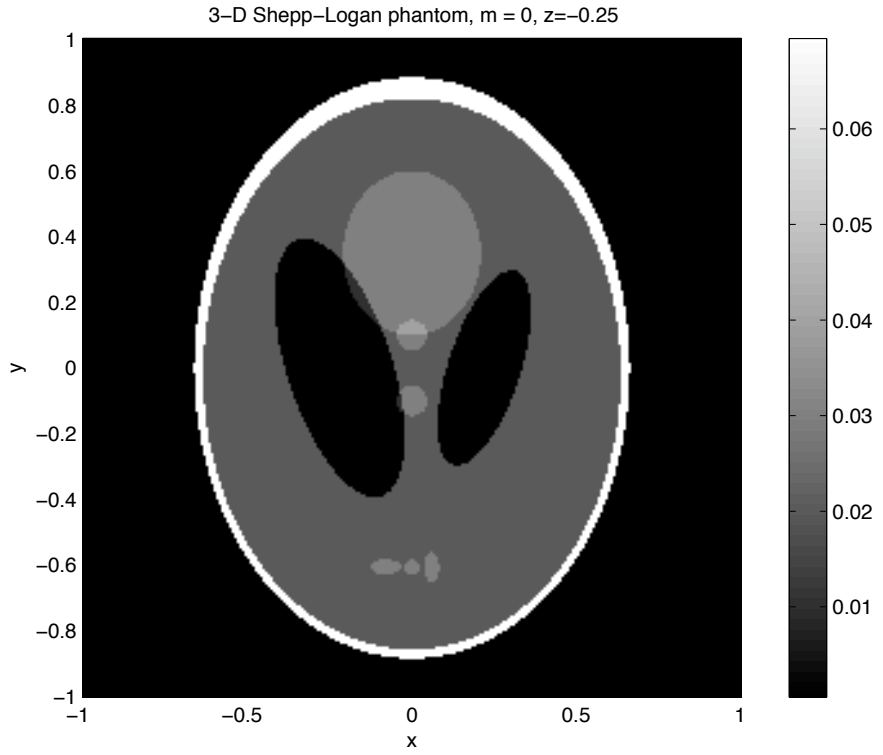

Figure 5.1: The slice z=-0.25 of the 3-D Shepp-Logan phantom

3-D phantom with $m = 0$ is shown in Figure 5.1. Note that the colormap has been rescaled to the range $[0, 0.07]$.

For experiments 2 throught 7, we use a phantom which consists of a single ellipsoid when $m = 0$. We also use the twice differentiable version of this phantom with $m = 3$. Note that the smallest ellipsoid in the Shepp-Logan phantom is much smaller than the one used in the single ellipsoid phantom. Since more rays pass through the larger ellipsoid, better estimates of the convergence rates can be obtained with the single ellipsoid phantom. The parameters for the second phantom are listed in Table 5.2. The phantom for $m = 0$ and $m = 3$ is shown in Figures 5.2 and 5.3 respectively.

a	b	c	x_0	y_0	z_0	β	τ
0.35	0.25	0.15	0.2	0.3	0.1	25	1

Table 5.2: Parameters for the single ellipsoid phantom

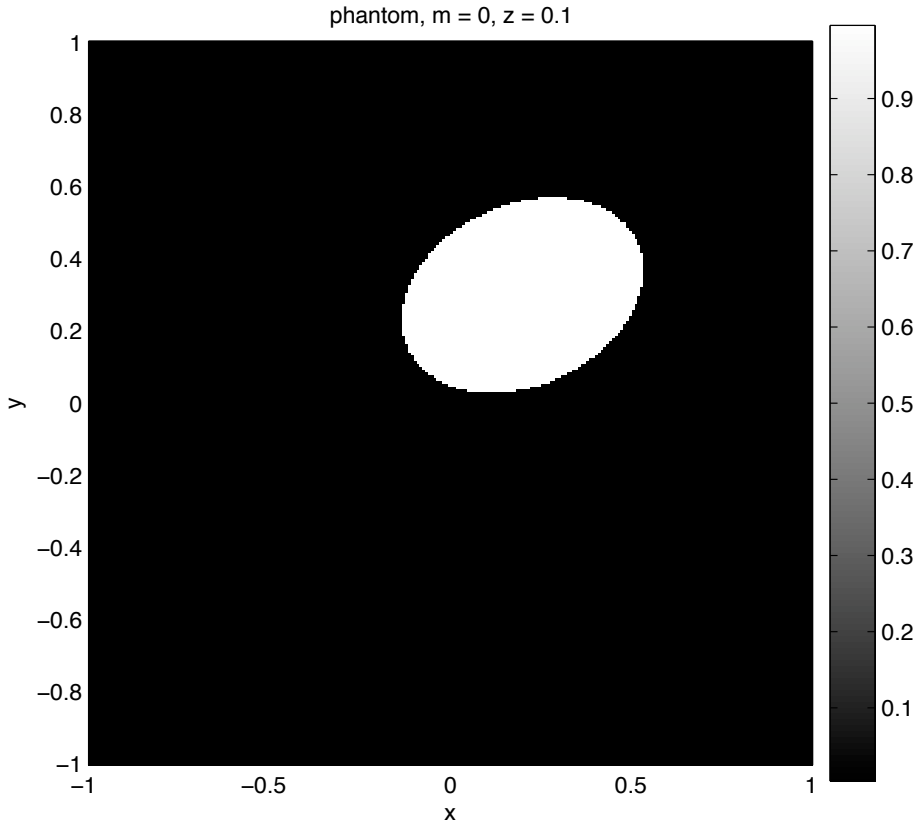

Figure 5.2: The slice $z = 0.1$ of the single ellipsoid phantom with $m = 0$

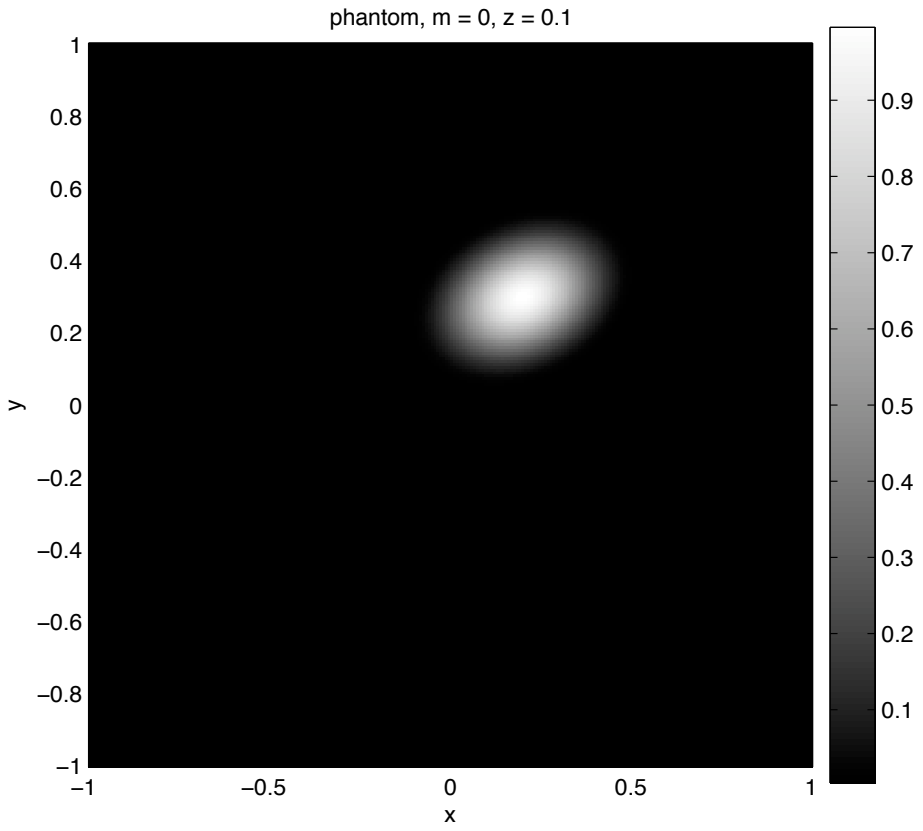

Figure 5.3: The slice $z = 0.1$ of the single ellipsoid phantom with $m = 3$

5.3 Numerical Experiments

Seven numerical experiments were performed on a desktop personal computer running Windows XP, with a 3.06 GHz Pentium 4 processor and 1 GB of RAM.

Experiment 1

In order to qualitatively compare the Katsevich and FDK algorithms, three different slices of the 3-D Shepp-Logan phantom were reconstructed: $z = 0$, $z = -0.1$, and $z = -0.25$. Reconstructions were computed for the Katsevich algorithm using both flat and curved detectors. The FDK reconstruction was for a flat detector only. The parameters used for the reconstructions are listed in Table 5.3. The reconstructed images for the three slices follow in Figures 5.4, 5.5, and 5.6. All images were made with a re-scaled color map in the range $[0, 0.07]$. Also, plots of the reconstructed attenuation profiles for the line $x = 0, z = -.25$ are provided in Figures 5.7-5.12.

Comparing the images, we see that the flat and curved Katsevich algorithms give qualitatively similar results. Although difficult to see from the pictures, the artifacts displayed by the Katsevich reconstructions lie on curves tangent to discontinuities. On the other hand, the artifacts displayed by the FDK reconstructions lie on straight lines tangent to discontinuities. In addition, the artifacts displayed by the FDK reconstructions are significantly higher outside of the skull than the artifacts for the Katsevich reconstructions.

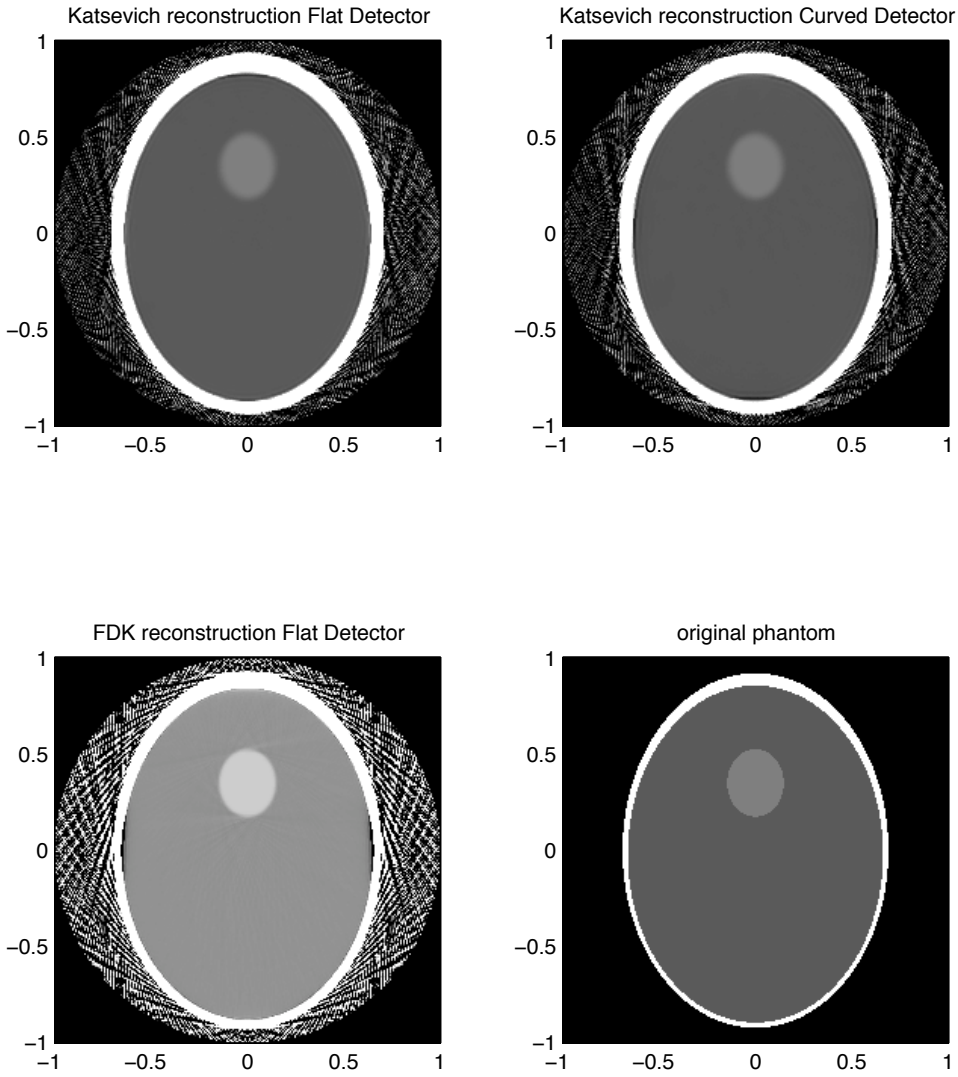

Figure 5.4: Experiment 1: The slice z=0

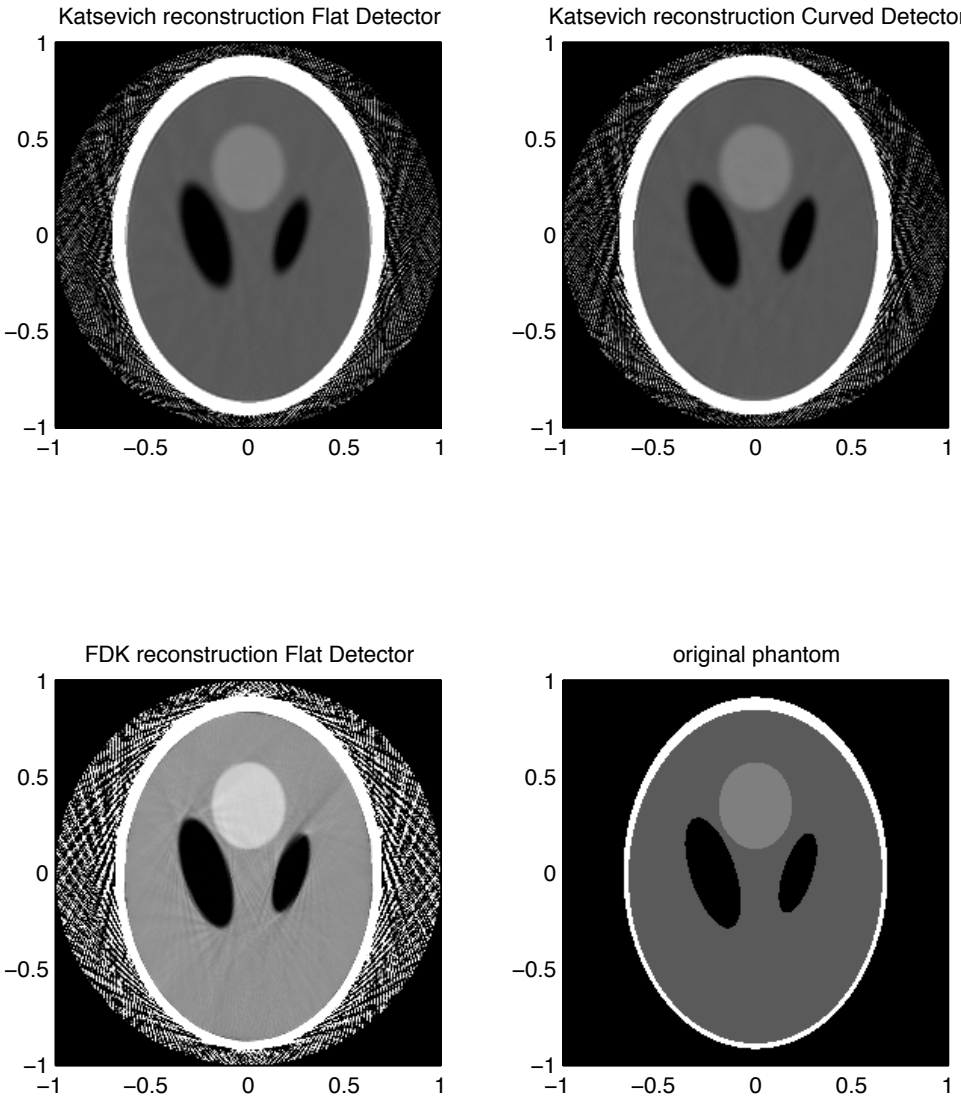

Figure 5.5: Experiment 1: The slice z=-0.1

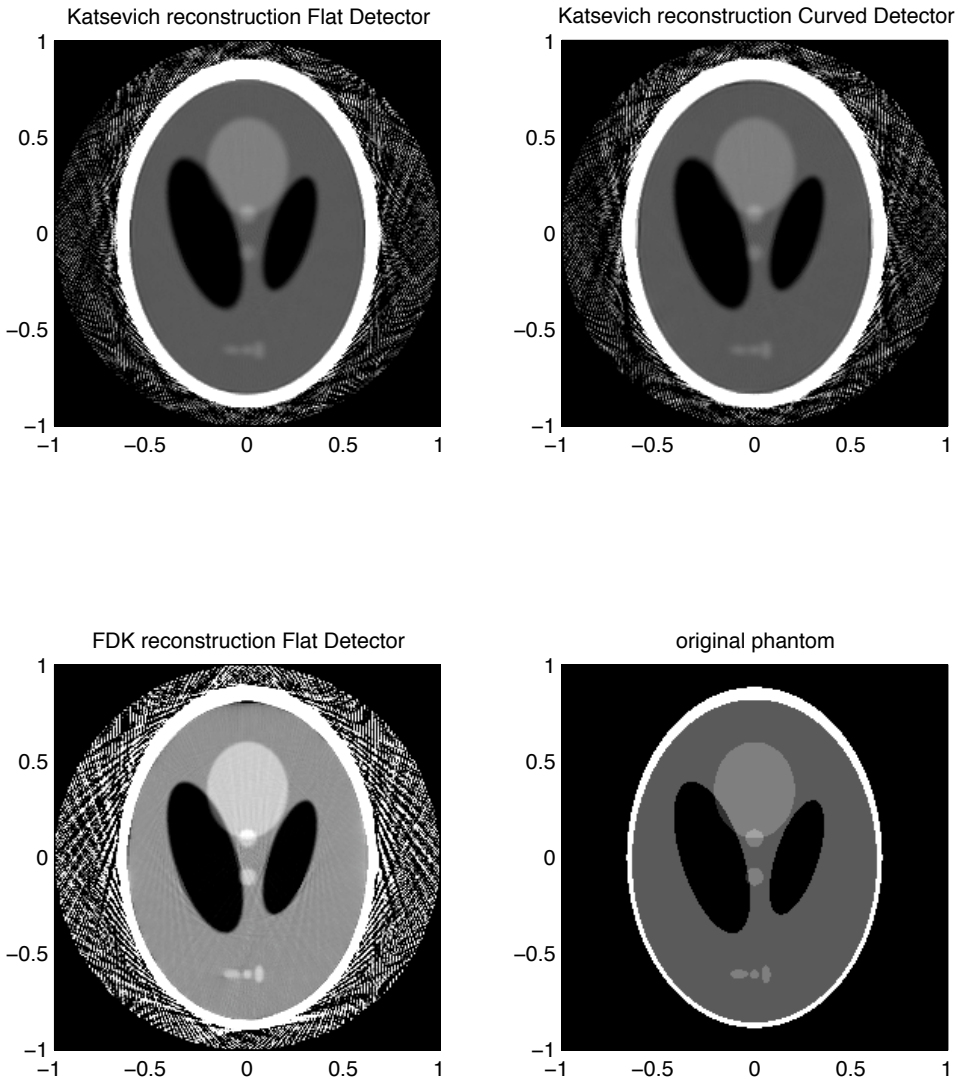

Figure 5.6: Experiment 1: The slice z=-0.25

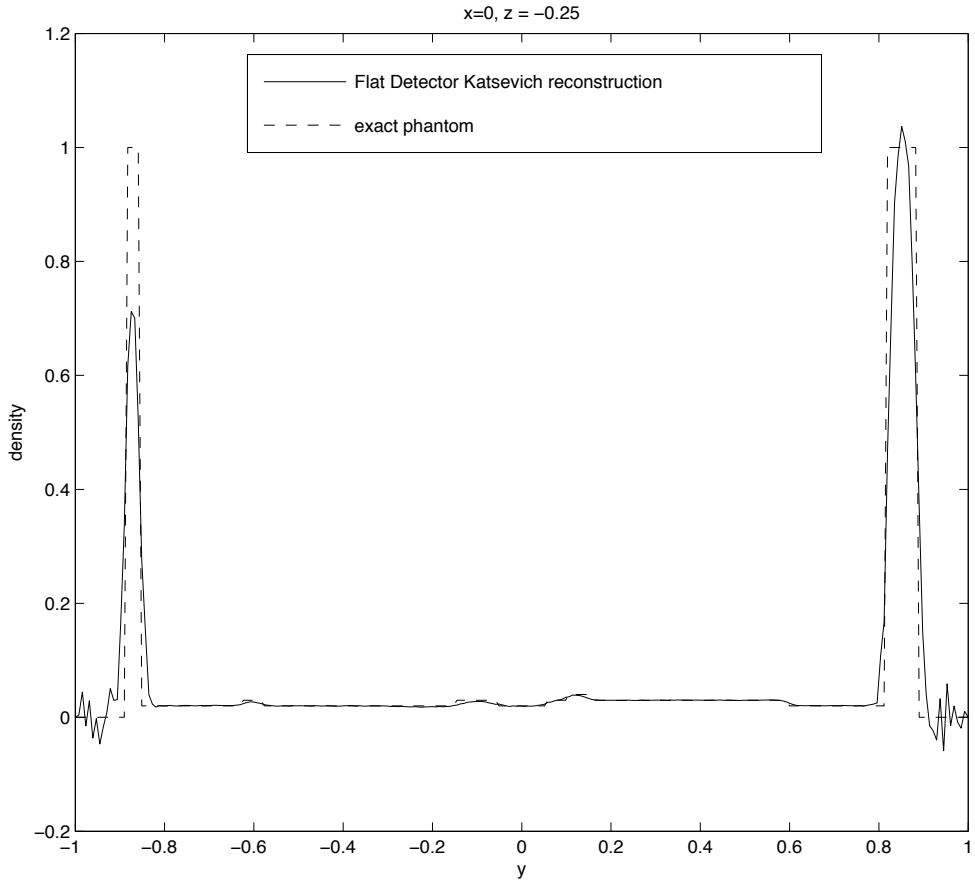

Figure 5.7: Experiment 1: Attenuation profile of the line $x = 0, z = -0.25$ for Katsevich method with flat detector

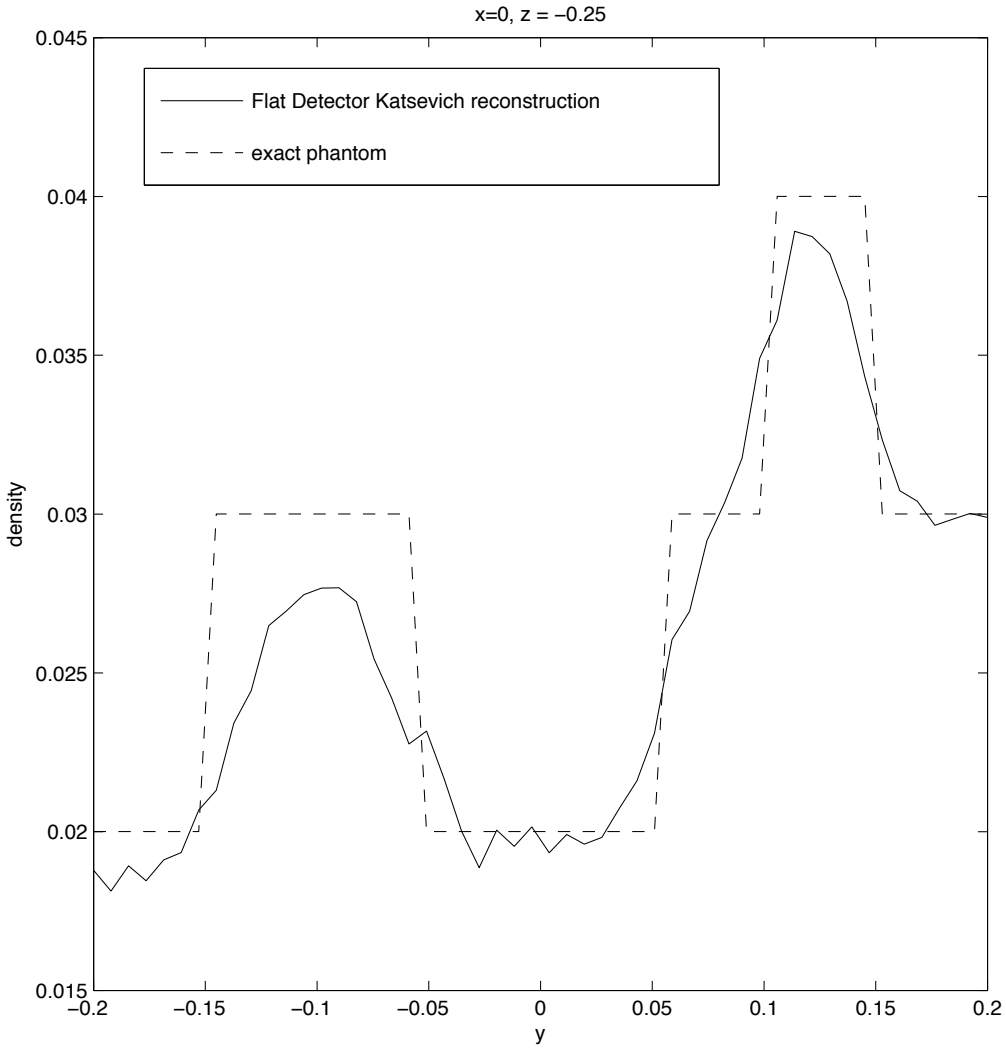

Figure 5.8: Experiment 1: Zoom of attenuation profile of the line $x = 0, z = -0.25$ for Katsevich method with flat detector

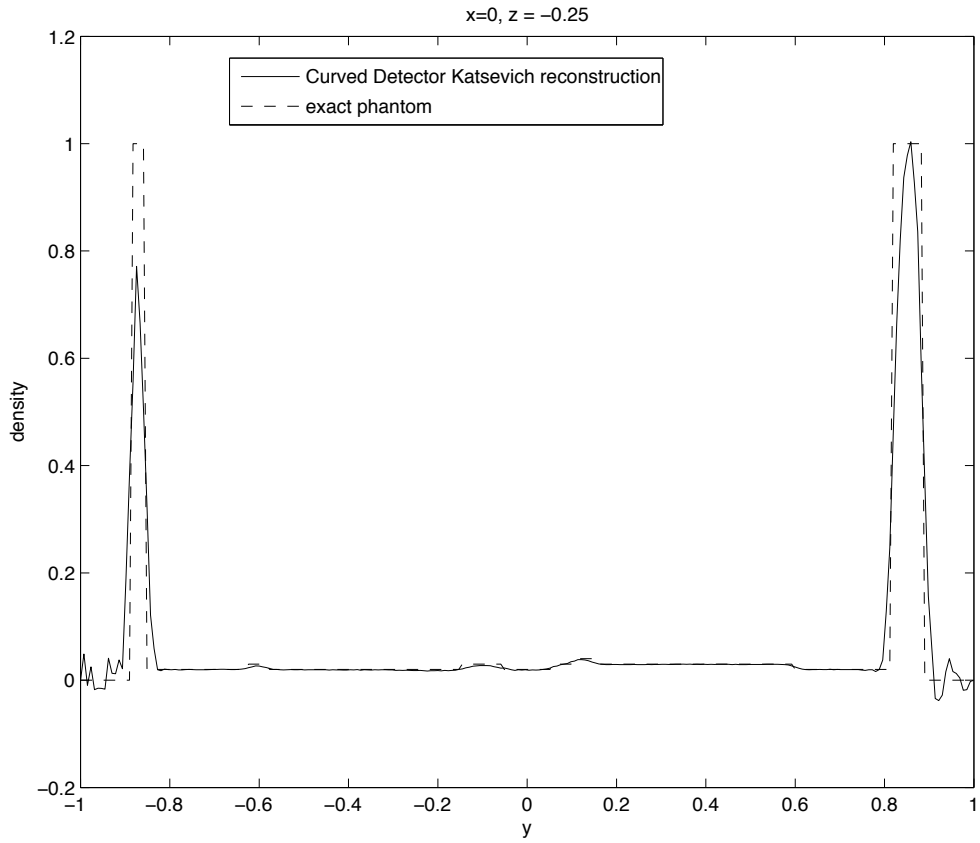

Figure 5.9: Experiment 1: Attenuation profile of the line $x = 0, z = -0.25$ for Katsevich method with curved detector

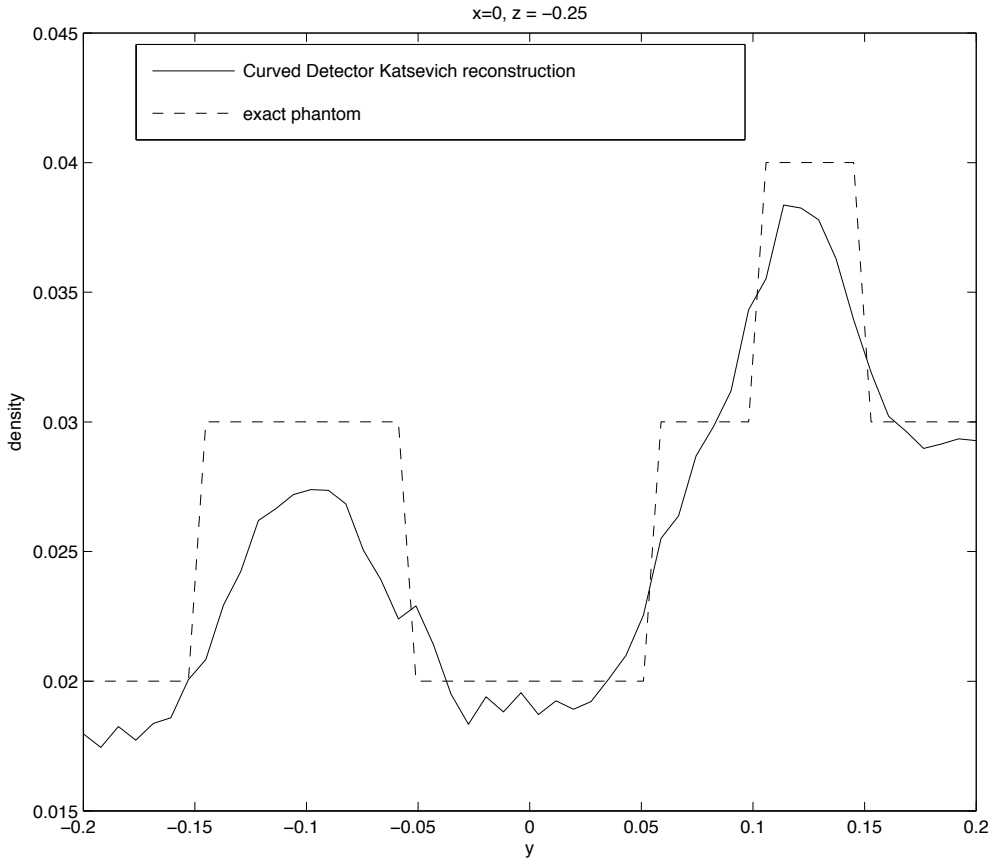

Figure 5.10: Experiment 1: Zoom of attenuation profile of the line $x = 0, z = -0.25$ for Katsevich method with curved detector

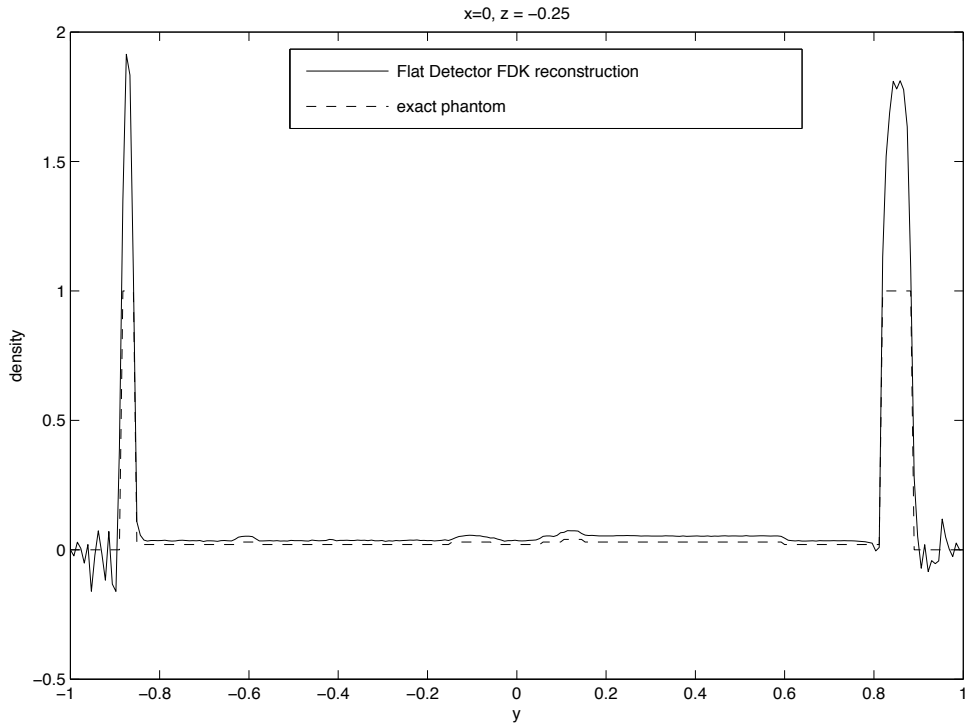

Figure 5.11: Experiment 1: Attenuation profile of the line $x = 0, z = -0.25$ for FDK method with flat detector

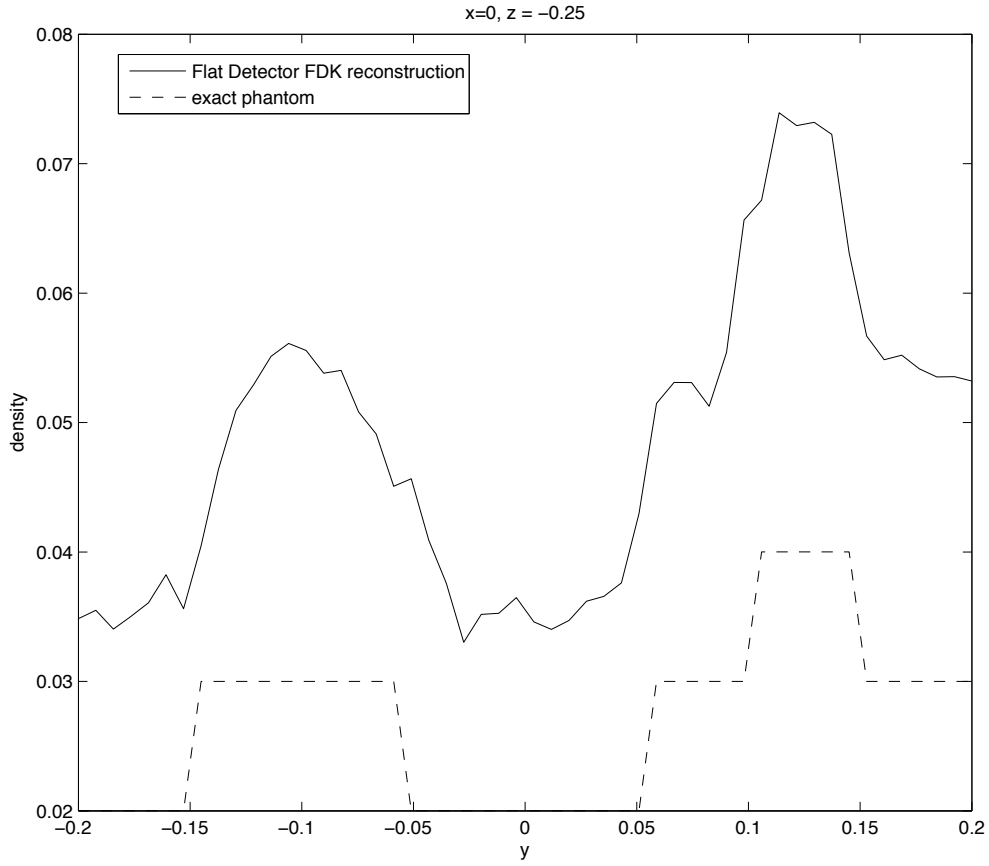

Figure 5.12: Experiment 1: Zoom of attenuation profile of the line $x = 0, z = -0.25$ for FDK method with flat detector

Reconstruction Size ($M_x \times M_y$)	256 x 256
Smoothness Parameter (m)	0
Detector Rows (M)	16
Detector Columns (N)	138
Detector Element Width ($\Delta u, D\Delta\alpha$)	0.0313
Detector Element Height (Δw)	0.0313
Number of Source Positions per Turn	256
Number of Filtering Lines (L)	64
Maximum Object Radius (r)	1
Helix Radius (R)	3
Source to Detector Distance (D)	6
Helical Pitch (P)	0.2740

Table 5.3: Parameters for Experiment 1

Experiment 2

This experiment compared the convergence behavior of the Katsevich and FDK methods using the single ellipsoid phantom. All reconstructions were for the slice $z = 0.1$. The total detector height was held constant as the number of detector rows was increased (Δw decreased). In addition, the number of source positions per turn and the number of filtering lines was increased as Δw decreased. The parameters used are listed in Table 5.4. Let $F[i, j]$ denote the reconstruction and let $P[i, j]$ denote the exact phantom. Then the relative l^2-error for each reconstructed slice was computed using the formula below:

$$\text{relative } l^2 \text{ error} = \sqrt{\frac{\sum_i \sum_j (P[i,j] - F[i,j])^2}{\sum_i \sum_j (P[i,j])^2}}. \tag{5.1}$$

The relative l^2-errors and reconstruction times are listed in Tables 5.5-5.7.

For the smooth phantom ($m = 3$), the relative l^2-error for the Katsevich method was observed to converge at asymptotic rates of $O(\Delta w^{0.1.97})$ and $O(\Delta w^{0.1.96})$ for the flat and curved detectors, respectively. On the other hand, the FDK method did not converge. However, note that for $M = 8$, the FDK method had a lower relative error than the Katsevich method.

For the discontinuous phantom ($m = 0$), the relative l^2-error for the Katsevich method was observed to converge at an asymptotic rate of $O(\Delta w^{0.57})$

for both flat and curved detectors. The FDK method did not converge.

The curved detector implementation for the Katsevich method was observed to have substantially larger execution times than the flat detector implementation. This time difference may be attributed to the fact that the curved detector implementation requires repeated evaluations of the MATLAB arctangent function during the backprojection step.

Experiment 3

This experiment compared the convergence behavior of the Katsevich and FDK methods, but with half the detector height and helical pitch of experiment 2. All reconstructions were for the slice $z = 0.1$ of the single ellipsoid phantom. For this experiment, it was not computationally feasible to compute the case of $M = 32$ detector rows, so only $M = 4$, $M = 8$, and $M = 16$ detector rows were considered. The parameters are listed in Table 5.8 and the results follow in Tables 5.9-5.11.

For the smooth phantom ($m = 3$), the relative l^2-error for the Katsevich method was observed to converge at an asymptotic rate of $O(\Delta w^{3.23})$ for the flat detector and $O(\Delta w^{3.36})$ for the curved detector. The FDK method did not converge. However, note that for $M = 4$, the FDK method had a lower relative error than the Katsevich method.

For the discontinuous phantom ($m = 0$), the relative l^2-error for the Katsevich method was observed to converge at asymptotic rates of $O(\Delta w^{0.75})$ and $O(\Delta w^{0.74})$ for the flat and curved detectors, respectively. Again, the FDK method did not converge but had lower relative error for $M = 4$.

Experiment 4

This experiment compared the convergence behavior of the Katsevich and FDK methods, with a ratio of object radius to helical radius of $r/R = 1/2$ (compare to experiments 2 and 3 which used $r/R = 1/3$). All reconstructions were for the slice $z = 0.1$ of the single ellipsoid phantom. The parameters are listed in Table 5.12 and the relative l^2-errors and reconstruction times are listed in Tables 5.13-5.15.

For the smooth phantom ($m = 3$), the relative l^2-error for the Katsevich method was observed to converge at asymptotic rates of $O(\Delta w^{1.86})$ and $O(\Delta w^{1.82})$ for the flat and curved detectors, respectively. The FDK method

did not converge. However, note that for $M = 4$, the FDK method had a lower relative error than the Katsevich method.

For the discontinuous phantom ($m = 0$), the relative l^2-error for the Katsevich method was observed to converge at an asymptotic rate of $O(\Delta w^{0.54})$ for both detectors, and the FDK method did not converge.

Experiment 5

This experiment varied the number of source positions per turn with all other settings constant. The setting were chosen to be the same as experiment 2 with M=16 and m=3. All reconstructions were for the slice $z = 0.1$ of the single ellipsoid phantom. The parameters used are listed in Table 5.16. The relative l^2 errors and reconstruction times are listed in Tables 5.17.

For the Katsevich method, the relative l^2 errors appear to saturate when the number of sources per turn is around 256. The FDK method saturates when the number of sources per turn is around 64.

Experiment 6

This experiment compared a small detector together with a small helical pitch to the case of a large detector together with a large helical pitch with the individual detector element size held constant. The small detector used 4 detector rows and the large detector used 32 detector rows. All reconstructions were for the slice $z = 0.1$ of the single ellipsoid phantom. The parameters used for this experiment are listed in Table 5.18. The relative l^2 errors and reconstruction times are listed in Tables 5.19.

It is very interesting to note that the Katsevich method gave much lower errors (especially for m=3) in the large detector/large pitch case. By comparison, the FDK method does not show much change in the relative errors for the two detector sizes.

Experiment 7

This experiment sought to further examine the small detector/small pitch case to better explain the results of experiment 6. All reconstructions were for the slice $z = 0.1$ of the single ellipsoid phantom. The total detector height was held constant as the number of detector rows and columns was

increased. The parameters used are listed in Table 5.20. The relative l^2 errors and reconstruction times are listed in Tables 5.21.

For the Katsevich method, as the detector element size decreased, the relative error decreased rapidly. On the other hand, the relative error for the FDK method increased quickly as the detector element size decreased.

Reconstruction Size ($M_x \times M_y$)	256 x 256
Smoothness Parameter (m)	0, 3
Detector Height	0.5
Detector Rows (M)	4, 8, 16, 32
Detector Columns (N)	36, 70, 138, 274
Detector Element Width (Δu, $D\Delta\alpha$)	0.1250, 0.0625, 0.0313, 0.0156
Detector Element Height (Δw)	0.1250, 0.0625, 0.0313, 0.0156
Number of Source Positions per Turn	64, 128, 256, 512
Number of Filtering Lines (L)	16, 32, 64, 128
Maximum Object Radius (r)	1
Helix Radius (R)	3
Source to Detector Distance (D)	6
Helical Pitch (P)	0.2740

Table 5.4: Parameters for Experiment 2

m	M	relative l^2 Error	time(sec)
0	4	.5248	6.0
0	8	0.2378	10.1
0	16	0.1546	26.9
0	32	0.1083	152.8
0	convergence order	$O(\Delta w^{0.57})$	$O(\Delta w^{-2.5})$
3	4	0.5920	6.0
3	8	0.1785	10.0
3	16	0.0433	27.0
3	32	0.0116	152.9
3	convergence order	$O(\Delta w^{1.97})$	$O(\Delta w^{-2.5})$

Table 5.5: Experiment 2: Katsevich method for flat detector errors and times

m	M	relative l^2 Error	time(sec)
0	4	.5082	26.1
0	8	0.2344	47.0
0	16	0.1551	97.6
0	32	0.1089	292.5
0	convergence order	$O(\Delta w^{0.57})$	$O(\Delta w^{-1.6})$
3	4	0.5570	26.8
3	8	0.1531	48.4
3	16	0.0358	103.6
3	32	0.0101	301.0
3	convergence order	$O(\Delta w^{1.96})$	$O(\Delta w^{-1.5})$

Table 5.6: Experiment 2: Katsevich method for curved detector errors and times

m	M	relative l^2 Error	time(sec)
0	4	0.6000	4.5
0	8	0.2136	8.8
0	16	0.7737	19.2
0	32	2.5367	58.0
0	convergence order	no convergence	$O(\Delta w^{-1.6})$
3	4	0.5956	4.5
3	8	0.1375	9.3
3	16	0.7642	19.3
3	32	2.5428	59.2
3	convergence order	no convergence	$O(\Delta w^{-1.6})$

Table 5.7: Experiment 2: FDK method for flat detector errors and times

Reconstruction Size ($M_x \times M_y$)	256 x 256
Smoothness Parameter (m)	0, 3
Detector Height	0.25
Detector Rows (M)	4, 8, 16
Detector Columns (N)	70, 138, 274
Detector Element Width ($\Delta u, D\Delta\alpha$)	0.0625, 0.0313, 0.0156
Detector Element Height (Δw)	0.0625, 0.0313, 0.0156
Number of Source Positions per Turn	128, 256, 512
Number of Filtering Lines (L)	32, 64, 128
Maximum Object Radius (r)	1
Helix Radius (R)	3
Source to Detector Distance (D)	6
Helical Pitch (P)	0.1370

Table 5.8: Parameters for Experiment 3

m	M	relative l^2 Error	time(sec)
0	4	.5484	11.3
0	8	0.1874	27.7
0	16	0.1113	137.3
0	convergence order	$O(\Delta w^{0.75})$	$O(\Delta w^{-2.3})$
3	4	0.5496	10.8
3	8	0.1223	27.5
3	16	0.0130	137.8
3	convergence order	$O(\Delta w^{3.23})$	$O(\Delta w^{-2.3})$

Table 5.9: Experiment 3: Katsevich method for flat detector errors and times

m	M	relative l^2 Error	time(sec)
0	4	.5414	45.8
0	8	0.1860	98.4
0	16	0.1117	279.1
0	convergence order	$O(\Delta w^{0.74})$	$O(\Delta w^{-1.5})$
3	4	0.5310	49.3
3	8	0.1146	101.4
3	16	0.0112	278.7
3	convergence order	$O(\Delta w^{3.36})$	$O(\Delta w^{-1.5})$

Table 5.10: Experiment 3: Katsevich method for curved detector errors and times

m	M	relative l^2 Error	time(sec)
0	4	0.2141	10.3
0	8	0.7750	21.4
0	16	2.5390	53.5
0	convergence order	no convergence	$O(\Delta w^{-1.3})$
3	4	0.1422	10.3
3	8	0.7601	21.3
3	16	2.5393	53.4
3	convergence order	no convergence	$O(\Delta w^{-1.3})$

Table 5.11: Experiment 3: FDK method for flat detector errors and times

Reconstruction Size ($M_x \times M_y$)	256 x 256
Smoothness Parameter (m)	0, 3
Detector Height	0.5
Detector Rows (M)	4, 8, 16, 32
Detector Columns (N)	40, 76, 150, 298
Detector Element Width ($\Delta u, D\Delta\alpha$)	0.1250, 0.0625, 0.0313, 0.0156
Detector Element Height (Δw)	0.1250, 0.0625, 0.0313, 0.0156
Number of Source Positions per Turn	64, 128, 256, 512
Number of Filtering Lines (L)	16, 32, 64, 128
Maximum Object Radius (r)	1
Helix Radius (R)	2
Source to Detector Distance (D)	4
Helical Pitch (P)	0.2109

Table 5.12: Parameters for Experiment 4

m	M	relative l^2 Error	time(sec)
0	4	0.4722	6.0
0	8	0.2329	10.6
0	16	0.1583	29.7
0	32	0.1103	170.1
0	convergence order	$O(\Delta w^{0.54})$	$O(\Delta w^{-2.5})$
3	4	0.5437	6.1
3	8	0.1718	10.5
3	16	0.0491	29.6
3	32	0.0131	173.5
3	convergence order	$O(\Delta w^{1.86})$	$O(\Delta w^{-2.5})$

Table 5.13: Experiment 4: Katsevich method for flat detector errors and times

m	M	relative l^2 Error	time(sec)
0	4	0.4986	26.4
0	8	0.2709	49.1
0	16	0.1841	103.3
0	32	0.1286	314.1
0	convergence order	$O(\Delta w^{0.54})$	$O(\Delta w^{-1.6})$
3	4	0.5855	27.4
3	8	0.2313	49.1
3	16	0.0672	101.6
3	32	0.0186	315.5
3	convergence order	$O(\Delta w^{1.82})$	$O(\Delta w^{-1.6})$

Table 5.14: Experiment 4: Katsevich method for curved detector errors and times

m	M	relative l^2 Error	time(sec)
0	4	0.2668	4.8
0	8	0.9934	9.3
0	16	2.9666	20.6
0	32	6.9493	64.5
0	convergence order	no convergence	$O(\Delta w^{-1.6})$
3	4	0.1390	4.8
3	8	0.9588	9.4
3	16	2.9665	20.8
3	32	6.9615	63.3
3	convergence order	no convergence	$O(\Delta w^{-1.6})$

Table 5.15: Experiment 4: FDK method for flat detector errors and times

Reconstruction Size ($M_x \times M_y$)	256 x 256
Smoothness Parameter (m)	3
Detector Height	0.5
Detector Rows (M)	16
Detector Columns (N)	138
Detector Element Width ($\Delta u, D\Delta\alpha$)	0.0313
Detector Element Height (Δw)	0.0313
Number of Source Positions per Turn	32, 64, 128, 256, 512
Number of Filtering Lines (L)	64
Maximum Object Radius (r)	1
Helix Radius (R)	3
Source to Detector Distance (D)	6
Helical Pitch (P)	0.2740

Table 5.16: Parameters for Experiment 5

method	Sources Per Turn	relative l^2 Error	time(sec)
Kat flat	32	0.1219	6.0
Kat flat	64	0.0594	8.9
Kat flat	128	0.0472	14.8
Kat flat	256	0.0433	27.3
Kat flat	512	0.0415	51.2
Kat curved	32	0.1178	19.2
Kat curved	64	0.0531	32.1
Kat curved	128	0.0401	57.0
Kat curved	256	0.0358	107.9
Kat curved	512	0.0336	209.9
FDK flat	32	0.7980	2.7
FDK flat	64	0.7653	5.1
FDK flat	128	0.7646	9.8
FDK flat	256	0.7642	19.2
FDK flat	512	0.7641	38.4

Table 5.17: Experiment 5: errors and times

Reconstruction Size ($M_x \times M_y$)	256 x 256
Smoothness Parameter (m)	0, 3
Detector Rows (M)	4, 32
Detector Columns (N)	216
Detector Element Width ($\Delta u, D\Delta\alpha$)	0.02
Detector Element Height (Δw)	0.02
Number of Source Positions per Turn	256
Number of Filtering Lines (L)	128
Maximum Object Radius (r)	1
Helix Radius (R)	3
Source to Detector Distance (D)	6
Helical Pitch (P)	0.0438, 0.4531

Table 5.18: Parameters for Experiment 6

method	m	M	relative l^2 Error	time(sec)
Kat flat	0	4	0.4119	49.5
Kat flat	0	32	0.1210	56.0
Kat flat	3	4	0.4009	48.7
Kat flat	3	32	0.0162	55.6
Kat curved	0	4	0.4095	123.0
Kat curved	0	32	0.1225	129.5
Kat curved	3	4	0.3963	123.3
Kat curved	3	32	0.0141	136.7
FDK flat	0	4	1.7718	22.1
FDK flat	0	32	1.7511	24.2
FDK flat	3	4	1.7716	22.1
FDK flat	3	32	1.6892	24.3

Table 5.19: Experiment 6: errors and times

Reconstruction Size ($M_x \times M_y$)	256 x 256
Smoothness Parameter (m)	3
Detector Height	0.08
Detector Rows (M)	4, 8, 16
Detector Columns (N)	216, 428, 852
Detector Element Width ($\Delta u, D\Delta\alpha$)	0.02, 0.01, 0.005
Detector Element Height (Δw)	0.02, 0.01, 0.005
Number of Source Positions per Turn	256
Number of Filtering Lines (L)	128
Maximum Object Radius (r)	1
Helix Radius (R)	3
Source to Detector Distance (D)	6
Helical Pitch (P)	0.0438

Table 5.20: Parameters for Experiment 7

method	M	relative l^2 Error	time(sec)
Kat flat	4	0.4009	48.7
Kat flat	8	0.0467	112.7
Kat flat	16	0.0028	369.7
Kat curved	4	0.3963	123.3
Kat curved	8	0.0445	196.3
Kat curved	16	0.0035	454.5
FDK flat	4	1.7716	22.1
FDK flat	8	4.552	27.9
FDK flat	16	10.1089	67.2

Table 5.21: Experiment 7: errors and times

Chapter 6

Summary and Conclusions

This paper gave an introduction to Katsevich's inversion formula for helical cone-beam CT and provided derivations of implementation details for both flat and curved detector geometries. Seven numerical experiments were carried out which compared the numerical properties of the Katsevich formula to the classical FDK formula.

Experiment 1 compared reconstructions of three slices of the 3-D Shepp-Logan head phantom. The Katsevich method was observed to yield slight curving artifacts tangent to large discontinuities in the phantom. This result was different than the artifacts exhibited by the FDK method, which were straight lines tangent to discontinuities.

All of the remaining experiments concerned reconstructions of the slice $z = 0.1$ of the single ellipsoid phantom.

In Experiments 2, 3 and 4, the convergence behavior of the Katsevich and FDK methods were compared for different helical pitches, detector sizes, and different ratios of the object radius to the helical radius (r/R). In all three experiments the FDK method did not converge. This was expected, since the FDK method is based on an approximate inversion formula. On the other hand, the theoretically exact (before discretization) Katsevich method was found to converge in all three experiments. The smooth phantom ($m = 3$) converged at rates varying between $O(\Delta w^{1.8})$ and $O(\Delta w^{3.3})$ and the discontinuous phantom ($m = 0$) converged at rates between $O(\Delta w^{0.5})$ and $O(\Delta w^{.75})$, depending on the helical pitch and detector size. In particular, experiment 3 demonstrated that the convergence rate increased when the helical pitch and detector size was halved.

Experiment 5 showed the saturation of the reconstruction error as the

number of source positions per turn was increased with all other parameters held constant (the other parameters were the same as experiment 2 with M=16).

Experiment 6 compared reconstructions made using a small detector with small helical pitch to reconstructions made using a large detector and large helical pitch. The individual detector element size was kept the same for both cases. Remarkably, the Katsevich method was considerably more accurate for the large detector/large pitch case. By comparison, the FDK method displayed similar accuracy for both situations.

Finally, experiment 7 further examined reconstructions using a small detector and small helical pitch. The pitch and detector size were the same as used for experiment 6, but the number of detector rows and columns were increased. This experiment showed that as the number of detector elements increased, the errors quickly became smaller. Therefore, the puzzling outcome of experiment 6 may be attributed to insufficient sampling of the detector area. Moreover, examination of the results from experiments 2-4 shows that the case of 4 detector rows performed poorly. Since in each case the maximum allowable pitch was used, we may conclude that using 4 detector rows with the maximum allowable helical pitch gives poor reconstructions when using the Katsevich formula.

The implementation and numerical studies of this paper are just a first step towards a better understanding of the Katsevich inversion formula. Suggestions for future work include analytical numerical analysis of the inversion formula, exploration of alternate implementation methods, examination of artifacts in the axial direction, and fully 3-D numerical studies of convergence.

Bibliography

[1] Kyle Champley. Katsevich inversion formula for 3-D helical tomography. Math 656 presentation notes (unpublished), Oregon State University, May 2006.

[2] Guang-Hong Chen. An alternative derivation of Katsevich's cone-beam reconstruction formula. *Medical Physics*, 30(12):3217–3226, December 2003.

[3] P.E. Danielsson, P. Edholm, J. Eriksson, and S.M. Magnusson. Towards exact reconstruction for helical cone-beam scanning of long objects. In D.W. Townsend and P.E. Kinahan, editors, *Proceedings of 1997 Meeting on Fully 3D Image Reconstruction in Radiology and Nuclear Medicine*, pages 141–4, Pittsburgh, PA, 1997.

[4] M. Defrise, F. Noo, and H. Kudo. A solution to the long object problem in helical cone-beam tomography. *Physics in Medicine and Biology*, 45:623–43, 2000.

[5] Adel Faridani. Fan-beam tomography and sampling theory. In *Proceedings of Symposia in Applied Mathematics*, volume 63, pages 43–66. American Mathematical Society, 2006.

[6] Adel Faridani. Math 656 lecture (unpublished). Oregon State University, Spring 2006.

[7] L.A. Feldkamp, L.C. Davis, and J.W. Kress. Practical cone-beam algorithm. *Journal of the Optical Society of America*, 1(6):612–619, June 1984.

[8] Frank Jones. *Lebesgue Integration on Euclidean Space*. Jones and Bartlett, Sudbury, MA, revised edition, 2001.

[9] Avinash Kak and Malcolm Slaney. *Principles of Computerized Tomographic Imaging*. Classics in Applied Mathematics. SIAM, Philadephia, 2001. First published by IEEE press in 1988.

[10] Alexander Katsevich. Analysis of an exact inversion formula for spiral cone-beam CT. *Physics in Medicine and Biology*, 47:2583–2598, 2002.

[11] Alexander Katsevich. Theoretically exact filtered backprojection-type inversion algorithm for spiral CT. *SIAM Journal of Applied Mathematics*, 62:2012–2026, 2002.

[12] Alexander Katsevich. An improved exact filtered backprojection algorithm for spiral computed tomography. *Advances in Applied Mathematics*, 32:681–697, 2004.

[13] Frank Natterer. *The Mathematics of Computerized Tomgraphy*. Classics in Applied Mathematics. SIAM, Philadelphia, 2001. First published by John Wiley and Sons in 1986.

[14] Frank Natterer and Frank Wübbeling. *Mathematical Methods in Image Reconstruction*. Monographs on Mathematical Modeling and Computation. SIAM, Philadelphia, 2001.

[15] Frederic Noo, Jed Pack, and Dominic Heuscher. Exact helical reconstruction using native cone-beam geometries. *Physics in Medicine and Biology*, 48:3787–3818, 2003.

[16] Elena Prestini. *The Evolution of Applied Harmonic Analysis*. Applied and Numerical Harmonic Analysis. Birkhäuser, Boston, 2004.

[17] K.C. Tam, S. Samarasekera, and F. Sauer. Exact cone-beam CT with a spiral scan. *Physics in Medicine and Biology*, 43:1015–1024, 1998.

[18] Heang K. Tuy. An inversion formula for cone-beam reconstruction. *SIAM Journal of Applied Mathematics*, 43(3):546–552, June 1983.

[19] Ge Wang, Tein-Hsiang Lin, Ping-chin Cheng, and Douglas M. Shinozaki. A general cone-beam reconstruction algorithm. *IEEE Trans. on Medical Imaging*, 12(3):486–496, September 1993.

[20] Yangbo Ye and Ge Wang. Filtered backprojection formula for exact image reconstruction from cone-beam data along a general scanning curve. *Medical Physics*, 32(1):42–48, January 2005.

[21] Shiying Zhao, Hengyong Yu, and Ge Wang. A unified framework for exact cone-beam reconstruction formulas. *Medical Physics*, 32(6):1712–1721, June 2005.